Zhang, W., Neville, R., Zhang, D., Scarpa, F., Wang, L., & Lakes, R. (2018). The two-dimensional elasticity of a chiral hinge lattice metamaterial. *International Journal of Solids and Structures*, *141-142*, 254-263. https://doi.org/10.1016/j.ijsolstr.2018.02.027

The two-dimensional elasticity of a chiral hinge lattice metamaterial

Wenjiao Zhang[a,b], Robin Neville[b], Dayi Zhang[c,b], Fabrizio Scarpa[b*], Lifeng Wang[d], Roderic Lakes[e]

[a]School of Engineering, Northeast Agriculture University, No.59 Mucai Street, Harbin, 150030, P.R. China
[b]Bristol Composites Institute (ACCIS), University of Bristol, Bristol BS8 1TR, UK
[c]School of Energy and Power Engineering, Beijng University of Aeronautics and Astronautics (BUAA), Beijing, 100191, P.R.China
[d]Department of Mechanical Engineering, State University of New York at Stony Brook, Stony Brook, New York 11794, USA
[e]Department of Engineering Physics, University of Wisconsin-Madison, 1500 Engineering Drive, Madison, WI 53706-1687

ABSTRACT

We present a lattice structure defined by patterns of slits that follow a rotational symmetry (chiral) configuration. The chiral pattern of the slits creates a series of hinges that produce deformation mechanisms for the lattice due to bending of the ribs, leading to a marginal negative Poisson's ratio. The engineering constants are modelled using theoretical and numerical Finite Element simulations. The results are benchmarked with experimental data obtained from uniaxial and off-axis tensile tests, with an overall excellent agreement. The chiral hinge lattice is almost one order of magnitude more compliant than other configurations with patterned slits and - in contrast to other chiral micropolar media - exhibits an in-plane shear modulus that closely obeys the relation between Young's modulus and Poisson's ratio in homogeneous isotropic linear elastic materials.

Keywords: lattice; metamaterial; chiral; elasticity; tension; shear

1. Introduction

Lattice metamaterials are currently being developed to create unusual deformation mechanisms and multifunctional capabilities [1][2] in a vast range of applications, from energy absorption through microbuckling instabilities [3][4] to wave propagation and vibration transmissibility reduction effects [5][6]. A subset of lattice metamaterials is constituted by solids with negative Poisson's ratio, also known as auxetic [7][8][9]. The unusual auxetic behavior is essentially achieved using specific cell topologies as re-entrant units, rotating rigid/semi rigid units, as well as chiral systems. Wojciechowski [10] has first suggested an auxetic chiral configuration based on rotating disks and nearest neighbor inverse n^{th} power interactions. Prall and Lakes [11] have formally developed a chiral structural honeycomb providing a theoretical and experimental in-plane Poisson's ratio of -1. This configuration consists in ligaments connecting two cylinders located on the opposite sides and ends, with each cylinder having 6 tangent ligaments at regular 60^o intervals. Chiral cellular solids have shown some peculiar features over conventional hexagonal honeycombs, because of the out-of-plane partial decoupling between compressive and transverse shear behavior between the cylinders and the ligaments [12][13]. Alternative chiral topologies consisting of rectangular or other

* Corresponding Author. Email: f.scarpa@bristol.ac.uk

geometrical forms, as well as 3-, 4- and 6-connected ligaments in chiral and anti-chiral lattices have been reported and investigated in recent years, both from a mechanical quasi-static and dynamics perspective [14]-[27]. Auxetic topologies of perforation and cuts have also risen to prominence with a plethora of perforation patterns, ranging from circular holes to ellipses or cuts, which may convert two-dimensional conventional materials into negative Poisson's ratio metamaterials. Bertoldi et al. [28] and Grima et al. [29] have developed pilot studies on auxetic metamaterials with circular and diamond shape perforations, respectively. Cho et al. [30] have generated continuous pattern transformations in a thin sheet of material by introducing fractal cuts with different motifs through rigid unit rotation. Gatt et al. [31] have proposed a novel auxetic hierarchical system based on the rotating rigid units mechanism that exhibits a wide range of properties including different sized pores that can open to various extents. Inspired by ancient geometric motifs arranged in square and triangular grids, Rafsanjani [32] has introduced a class of switchable architected materials exhibiting simultaneous auxeticity and structural bistability by using a network of rotating units connected with compliant hinges. The use of slits/cuts following deterministic Kagome-types and various centre-symmetric topologies [33]-[36], as well as random patterns [37] has also been adopted to create 2D mechanical metamaterials.

In this paper, we present a lattice configuration with patterns of cuts that generate internal rotations through the creation of hinges and a structural chiral configuration. Chiral topologies are commonly developed by connecting ribs tangentially to cylinders or quadratic units [11][16]. This involves the use of relatively complex manufacturing techniques, ranging from 3D printing [12] to composites bonding techniques [38]. Moreover, the relative porosities of these chiral lattices are quite large, and most of the structural chiral honeycombs have maximum relative densities around 12% [39]. By contrast, the new 2D chiral lattice hinge configuration presented in this work is created by a self-similar generation of a series of cuts, which resembles the first iteration of a Peano's curve [40]. The pattern proposed in this work also follows the layout of the cross-chiral topology [41]. In this lattice the hinge effects are due to flexure of the ribs. The width of the perforations used in this lattice is negligible compared to the shortest length of the unit cell, and that allows creating a structure with chirality and extremely low porosity. The presence of a pattern of cuts leads to the use of laser or other more traditional cutting techniques, and also to a broad range of two-dimensional material substrates for producing the new lattice topology. In this paper, the equivalent in-plane engineering constants of the lattice are modelled using a combination of theoretical and finite element numerical techniques. The models are validated by experimental results obtained from uniaxial tensile and shear tests performed according to ASTM standards.

2. Theoretical model

2.1 Geometry

The fundamental unit cell of the chiral hinge lattice is shown in Figure 1. The square configuration can be described by using the parameters *a*, *b*, *t* and *h*. The parameter *a* represents the total length of the unit cell, *b* is thickness of the ribs, *t* is the width of the slit and *h* is the out-plane thickness of the unit cell (not indicated in the figure). The total length of the unit cell is $a=n\times(b+t)$, where *n* is an even integer (10 in cell represented in Figure 1). For simplification, the value of the gap *t* is neglected in the theoretical model developed in this work. For the purpose of the numerical model described later, the gap *t* is equal to *b*/10 and consistent with the cutting parameters adopted in the fabrication of the experimental samples.

2.2 In-plane tensile modulus

The lattice structure is considered as behaving as an equivalent isotropic and linear elastic in-plane material. The square representative unit cell (RUC) of the lattice structure is constituted by 36 beam Euler-Bernoulli components. For the case of the in-plane uniaxial tensile loading, the boundary conditions are representative of a clamp located at the corner, and a uniform load intensity *q* applied to the interface with an adjacent cell (Fig.2 (a)). To simulate the deformation of the chiral hinge lattice, the whole unit cell is represented as a closed, sequential and statically indeterminate beam structure, in which the uniform loading *q* is substituted by a concentrated force *P* (Fig.2 (b)). To solve for the internal forces within the resulting closed and hyperstatic beam structure, the corner between the beam components 1 and 36 is cut open; the boundary condition is then set as a fixed end of beam number 36 (Fig.2 (c)). The calculation of internal force equations for the whole RUC starts at beam number 1. The recurrent formulas for the internal normal (F_{Ni}) and shear (F_{si}) forces and bending moments M_i are: $F_{N1}(x_1)=-F_y$, $F_{s1}(x_1)=-F_x$, $M_1(x_1)=M-F_x\times x_1$. The other beam components can be then calculated from the previous beams in the sequence of elements. As an example, for the case of the configuration corresponding to $a=10b$ (Fig. 2), the the axial force and shear forces of the i^{th} beam are expressed as: $F_{Ni}(x_i)=F_{si-1}$, $F_{si}(x_i)=F_{Ni-1}$, $M_i(x_i)=M_{i-1}(l_{i-1})\pm F_{Ni-1}\times x_i$ (with *i*=2..18.18a..36). For this particular configuration, one can also state that $F_{N19}(x_{19})=F_{N18a}$, $F_{s19}(x_{19})=F_{s18a}-P$, and $M_{19}(x_{19})=M_{18a}(l_{18a})-F_{s18a}\times x_{19}+P\times x_{19}$. As a consequence, three complementary conditions ($\delta_1^x=0, \delta_1^y=0, \delta_1^\theta=0$) are imposed to solve the unknown internal forces F_x, F_y, M of the beam element in the hyperstatic structure.

We then apply Castigliano's theorem by simultaneously considering three types of strain energies associated to bending, tensile and shear loading:

$$U=\sum_{i=1}^{n}\left(\int_0^{l_i}\frac{M_i^2(x)}{2EI_z}\mathrm{d}x+\int_0^{l_i}\frac{F_{Ni}^2(x)}{2EA}\mathrm{d}x+k\int_0^{l_i}\frac{F_{Si}^2(x)}{2GA}\mathrm{d}x\right) \quad (1)$$

In (1) *E* is the Young's modulus of core material, *G* is the shear modulus of the material ($G=E/\big(2(1+\nu)\big)$), $k=\big[10(1+\nu)\big]/(12+11\nu)$ is the Timoshenko shear coefficient for a

rectangular cross section with core Poisson's ratio v [41], $I_z = hb^3/12$ is the second moment of area and $A=bh$ is the area of the cross section of each beam element. Within the context of this work, we define as core the substrate material of the lattice.

According to the Castigliano's theorem, the displacement of a beam under the influence of a force P may be expressed as:

$$\delta = \frac{\partial U}{\partial P} \tag{2}$$

Therefore, the total strain energy of the chiral hinge cell under a uniaxial tensile loading P is obtained as:

$$U = \frac{P^2}{Eh} \times \frac{\sum_{i=0}^{6} B_i v^i}{\sum_{i=0}^{5} C_i v^i} \tag{3}$$

Where B_i and C_i are constants. From Eq. (2), displacement δ_x under the uniaxial tensile loading P is obtained as

$$\delta_x = \frac{2P}{Eh} \times \frac{\sum_{i=0}^{6} B_i v^i}{\sum_{i=0}^{5} C_i v^i} \tag{4}$$

The effective Young's modulus E_x^* is defined as the ratio between the nominal stress and the strain:

$$E_x^* = \frac{\sigma_x}{\varepsilon_x} = \frac{P}{A}\frac{1}{\delta_x / L_x} = \frac{P}{L_y h}\frac{1}{\delta_x / L_x} = \frac{PL_x}{\delta_x L_y h} \tag{5}$$

in which L_x, L_y, h and A are the initial lengths along the x and y directions, the out-plane thickness and the cross-sectional area of the unit cell structure, respectively.

Therefore, the homogenized non-dimensional effective elastic modulus of the chiral hinge lattice along the loading direction is given by:

$$\frac{E_x^*}{E} = \frac{1}{2} \times \frac{\sum_{i=0}^{5} C_i v^i}{\sum_{i=0}^{6} B_i v^i} \tag{6}$$

2.3 In-plane Poisson's ratio

The overall Poisson's ratio v_x is defined as the ratio between the transverse strain and the longitudinal one along the direction of the tensile loading and is then written as [43]:

$$v_x = -\frac{\varepsilon_y}{\varepsilon_x} = -\frac{\delta_{y2} - \delta_{y1}}{L_y}\frac{1}{\delta_x / L_x} = \frac{L_x\left(\delta_{y1} - \delta_{y2}\right)}{\delta_x L_y} \tag{7}$$

In Eq. (7), δ_x is the tensile displacement along the x direction; δ_{y1} and δ_{y2} are the average displacements for the nodes at the bottom and top ends along the y direction. Both δ_{y1} and δ_{y2}

are scalars. From Eq. (2), the vertical displacements generated by the bending moment and the axial and shearing forces at each single beam of the RUC can be calculated as follows:

$$\delta_{yi} = \pm \begin{cases} \dfrac{\partial(U_{Si} \pm U_{Mi})}{\partial P}, i = 2,4,6...36,18a \\ \dfrac{\partial U_{Ni}}{\partial P}, i = 1,3,5...35 \end{cases} \tag{8}$$

The total vertical displacements on the upper and lower edges of the unit cell are obtained as $\delta_{y2} = \sum \delta_{yi}$, $i = 1..18,18a$ and $\delta_{y1} = \sum \delta_{yj}$, $j = 19..36$. Substituting the values of δ_{y1} and δ_{y2} into Eq. (7), the overall effective Poisson's ratio v_x^* is obtained as:

$$v_x^* = \frac{1}{2} \times \frac{\sum_{i=0}^{5} D_i v^i}{\sum_{i=0}^{6} B_i v^i} \tag{9}$$

Where B_i and D_i are constants.

2.4 In-plane shear modulus

Three major types of fixtures are used to simulate an in-plane shear test: (a) uniaxial loading (loaded in diagonal tension), (b) biaxial (under tension and compression loads) and (c) tangential (cantilever and Wagner beams, rail shear fixture), shown in Fig. 3. However, only biaxial loading introduces as close as possible a pure shear deformation field [43]. We therefore use in this paper biaxial shear loading for both the theoretical modelling and the FE simulations.

In analogy to the uniaxial tensile modelling, the biaxial shear RUC for a=10b consists of 36 beams with uniform loading q_x, q_y, and boundary conditions as shown in Fig.4 (a). To simulate the deformation of the square unit cell each beam neutral axis is connected to create a closed, sequential and statically indeterminate single beam structure. Taking again as an example the chiral hinge lattice configuration of a=6b, the boundary conditions are further simplified as fixed-ends to beams 1 and 36. These BCs lead to the solution of the internal axial forces F_N , the shear force F_s and bending moment M . The uniform loading q_x, q_y are substituted by concentrated forces P_x and P_y (Fig.4 (b)). In a similar fashion to the uniaxial tensile case, complementary equations($\delta_1^x = 0$, $\delta_1^y = 0$, $\delta_1^\theta = 0$ and $\delta_{28}^x = 0$, $\delta_{28}^y = 0$) are imposed to obtain the unknown internal forces F_x , F_y , M of the beam #1, as well as the unknown reaction forces F_{x28} , F_{y28} in beam #28.

The total strain energy of the chiral unit cell under the biaxial loading P_x and P_y is given by:

$$U = \frac{1}{hE} \times \left(\frac{\sum_{i=0}^{42} \left(\alpha_i P_x^2 + \beta_i P_y^2 + \gamma_i P_x P_y \right) \nu^i}{\sum_{i=0}^{41} \zeta_i \nu^i} \right) \tag{10}$$

Where α_i, β_i, γ_i, ζ_i are constant and $\gamma_{42} = 0$. From Eqs. (10) and (2) the displacements δ_x and δ_y along the *x* and *y* directions are then determined. The expression for the effective shear modulus is represented as [39]:

$$G = \frac{\tau}{\gamma} = \frac{\sigma_x - \sigma_y}{2(\varepsilon_x - \varepsilon_y)} = \frac{P_x L_x - P_y L_y}{2h(\delta_x L_x - \delta_y L_y)} \tag{11}$$

From Eq. (11), the homogenized non-dimensional effective shear modulus of the chiral lattice hinge microstructure is expressed as:

$$\frac{G_x^*}{E} = \frac{(P_x + P_y)}{2} \times \left(\frac{\sum_{i=0}^{41} \zeta_i \nu^i}{\sum_{i=0}^{42} \left(\eta_i P_x + \lambda_i P_y \right) \nu^i} \right) \tag{12}$$

Where ζ_i, η_i and λ_i are constants.

3. The Finite Element model

To validate the in-plane linear elastic properties of the chiral hinge lattice structure, Finite element simulations have been performed using the commercial software ANSYS Rel. 14.0. The models have been developed using PLANE183 elements with 8 or 6 nodes and two translational degrees of freedom. The elements are well suited for modelling irregular meshes [44]. The FE RUC has a length of 20 mm with the width of the slits of 0.2 mm. The dimensions of the slits are the same of the nominal ones created through laser cutting the experimental samples. Boundary conditions are shown in Fig.5 for in-plane simulation.

Convergence test was also applied with four different types of models, in which different overall element sizes and different mesh methods at corners have been developed, shown in **Error! Reference source not found.** 6. Because of its symmetry, the moduli of elasticity and the Poisson's ratio are determined using one quarter of the RUC structure.

A detailed description for the models and the corresponding results are shown in **Error! Reference source not found.**. Model D (the one with the highest number of DOFs) is taken as the benchmark for all the other configurations ('Relative value' in Table 1). Considering both the accuracy and the computational efficiency, the model B is chosen for the following simulations. The cell related to Model B is also used to determine the sufficient number of cells to generate a lattice array and obtain accurate results. **Error! Reference source not found.** 7 shows that the values for both E_x^* and ν_x^* tend to converge for increasing numbers of unit cells,

and a model consisting of 8×8 Model-B cells is considerate adequate for the full-scale FE simulations at this stage.

4. Manufacturing and experimental tests

The lattice specimens have been produced by using a laser cutting facility to pattern PMMA substrates (World Lasers LR1612 laser cutter with a 40W CO_2 laser). The elastic mechanical properties of the PMMA material have been determined following the ASTM D638-08 standard. The tests have been performed using a Shimadzu Machine (10 KN load cell, 1 mm/min) with dog-bone specimens (Type I, T=6mm). The PMMA specimens have a Young's modulus of 2.23 GPa and a Poisson's ratio v=0.37±0.02. These properties have been used both for the analytical and FE simulations. A CAD model of the chiral hinge lattice has then been exported to the laser cutting machine to generate a 2D rotational symmetric chiral congiguration. The dimensions of each RUC have a width b = 2 mm and thickness h = 6 mm. The dimensions of the uniaxial tensile test samples are 190mm×100mm×6 mm (Fig. 8(a)). An off-axis 45° tensile test has been performed to determine the homogenized in-plane shear modulus following the ASTM D3518/D3518M-13 standard. The dimensions of the shear test samples are 243mm×108mm×6mm (Fig. 10(b)). At least five unit cells along the width and length of the samples have been included in the design of the two classes of specimens.

The in-plane tensile tests of the chiral hinge lattice samples were performed using a Shimadzu test machine with a 1 kN load cell and a constant displacement rate of 2 mm/min. An Imetrum video gauge system was used to track the strain fields along the loading and the transverse directions. Speckle patterns were placed on the samples with a black marker pen as tracking targets to improve the accuracy of the data acquisition from the video gauge system. We use in this work the incremental Poisson's ratio definition [45]:

$$v_{12} = -\frac{\mathrm{d}\varepsilon_{transverse}}{\mathrm{d}\varepsilon_{longitudinal}} \tag{13}$$

As the unit cell is a square configuration of rotational symmetry, the tensile test along the x direction is the same as that along the y direction. The in-plane shear modulus is calculated from the following expression [43][46]:

$$G_{12} = \frac{P_x}{2bh\left(\varepsilon_x - \varepsilon_y\right)} \tag{14}$$

in which b and h are the width and the thickness of the chiral hinge lattice specimen. The loading force is P_x, ε_x and ε_y are the strains along loading and transverse directions.

The determination of the in-plane Poisson's ratio follows the procedure outlined in [45], from which it is possible to calculate the variations of the cell dimensions. Firstly, the original raw experimental data of the transverse and longitudinal strains $\varepsilon_{transverse}$ and $\varepsilon_{longitudinal}$ related to one unit cell are obtained using a video gauge (Fig. 9(a)). Due to the resolution of the images extracted from the video gauge system noise is present in the data, a quadratic polynomial curve

was fitted to eliminate the noise and allow the Poisson's ratio to be sampled (Fig.11 (b)). The R^2 values of the fitting related to the four specimens are close to 1. Data from Specimen 1 have been discarded because of outliers. Then, Poisson's ratios of the four specimens were calculated according to Eq (13). The final effective Poisson's ratio behavior of one central unit cell with corresponding standard deviation for the four specimens was then obtained and shown in Fig. 10. Poisson's ratio is a ratio of transverse strain (Fig. 9) to longitudinal strain. The transverse strain values contain noise. Therefore noise related experimental uncertainty in the calculated Poisson's ratio (Fig. 10) is larger at small strain than at large strain.

5. Results and Discussion

Table 2 shows the comparisons between the theoretical modelling, the FE homogenization and the experimental results from the uniaxial and off-axis tensile loading. The experimental incremental Poisson's ratio has been derived for a tensile strain of 1.7%. The analytical tensile modulus E_x^* differs from the experimental result by 2.6%, while the FE ones are 6.5% softer than the modulus derived from the tensile tests. The experimental Poisson's ratio is 1.52% lower than the theoretical value, and even less when considering the FE result. For short specimens, there might be some concern about Saint Venant end effects, but since the magnitude of the Poisson's ratio is rather small such effects are likely minimal. The experimental values for the in-plane shear modulus G_x^* show higher discrepancies with the theoretical model (8.4%) and the FE results (5%). The theoretical in-plane shear modulus also shows a 3.5 % difference with the results from the FE simulations. Uncertainties affecting the results among the three sets of data can be ascribed to a variety of reasons. Aside from the uncertainties associated with the boundary conditions effectively applied to the experimental model, the main discrepancy related to the shear is the difference between the biaxial loading and the off-axis experimental tensile test performed. Even when the fixtures produce a pure shear deformation as closely as possible to the ideal case, there are still differences between a pure shear deformation and an approximated one [39]. Viscoelastic effects may be pertinent as well; a given displacement rate corresponds to different strain rate in specimens that are not the same length and geometry. Nonetheless, it is possible to observe a general very good agreement between the different models and the experimental results, and this gives confidence to the theoretical framework developed.

By inspecting equations (6), (9) and (12) it is possible to evince a dependency and sensitivity of the engineering constants versus the Poisson's ratio of the core material, as well as the width b and thickness h of the chiral hinge lattice. A sensitivity analysis versus the latter two geometry parameters indicate – as expected – that the width and thickness do not provide any contribution to the stiffness and Poisson's ratio of the lattice. The dependency versus the core material Poisson's ratio v is more marked. The non-dimensional Young's and shear moduli E_x^*/E and G_x^*/E tend to decrease linearly from a maximum value at $v = 0$, but exhibit a drop

of only 1.85% when passing to $\nu = 0.5$. The effective Poisson's ratio of the chiral lattice ν_x^* has however an opposite behavior with the variation of ν. For $\nu = 0$ one obtains a more negative Poisson's ratio $\nu_x^* = -0.042$, while for $\nu = 0.5$ the effective Poisson's ratio of the chiral lattice increases to -0.041. All these values however show that the dependency of the engineering constants versus the core Poisson's ratio is weak. The lattice exhibits a more significant dependence versus the aspect ratio *a/b* of the internal slits to ribs (Fig. 11).

A comparison of the analytical and FEA simulations related to the non-dimensional effective moduli are presented in Fig. 14(a)-(c). Within the analytical results we differentiate the contribution of the axial (A), shear (S) and bending (B) deformations in the ribs composing the chiral hinge lattice. The FEA results are related to the 8×8 cells model. From Fig. 14 it is possible to evince that the analytical model provides consistent results with the high-fidelity FE simulations for aspect ratios *a/b* higher than 6. In terms of non-dimensional stiffness, the shear deformation within the ribs tends to be responsible for higher Young's and shear moduli values. This is particularly evident for the lowest aspect ratio considered in this work (the *a/b*=6 structure), in which the neglect of the bending deformation gives rise to an increase of the Young's modulus by a factor of ~ 3.1 compared to the FE case, and by ~ 2.7 times for the shear modulus. High aspect ratios lead to a decrease of the stiffness, with the natural logarithm of E_x^*/E and G_x^*/E linearly proportional to $(a/b)^{-1}$. Regarding the Poisson's ratio, it is interesting to notice that the shear deformation contributes to maintain a ~ 0 ν_x^* effect; on the contrary, the bending tends to increase the negative Poisson's ratio effect at lower *a/b* ratios (Fig. 14(c)). It is worth noticing that by considering bending and axial deformations only, one can already obtain an excellent agreement with the FE results for *a/b* higher or equal than 10. Also in this case, discrepancies with the high-fidelity FE appear for the case $a/b = 6$, for which bending and stretching tend to provide a very low shear stiffness and negative Poisson's ratio behaviour that counteracts the stiffening effect given by the shear deformation mechanism.

The chiral lattice hinge structure is marginally auxetic. The negative Poisson's ratio effect is created through the hinging of the ribs, in a similar manner to the one observed in cross-chiral configurations [54]. The magnitude of the Poisson's ratio is extremely small (and close to zero) for the *a/b* range considered, but its negative value puts the lattice structure described in this work within the wider class of negative Poisson's ratio materials. This is not surprising, because the lattice configuration has similarities with chiral structural topologies that exhibit an in-plane negative Poisson's ratio behaviour [10][11][19][26]. Zero in-plane Poisson's ratio has been observed in cross-chiral configurations made from slender beams [41], for which the uniaxial-rotational coupling is the main deformation mechanism. It is worth noticing here that the marginal near zero Poisson's ratio is effectively encountered in the configurations corresponding to the presence of the slenderest ribs. On the contrary, for lower *a/b* values the main deformation mechanism of the ribs is the shear deformation of the cross section. The decrease of the stiffness provided by the patterns of cuts on the planar bulk material is also remarkable (~ 0.16% of the core for $a/b = 10$). The chiral hinge lattice is therefore more

compliant than the slit perforated systems with deterministic and random patterns, which exhibit non-dimensional stiffness between ~ 4% and 14% [34][35]. Another aspect worth mentioning is the behavior of the in-plane shear modulus. Under isotropic Hooke's law the shear modulus can be expressed as $G_1 = E_x^* \Big/ \left[2(1+\nu_x^*) \right]$. Although the material is structurally cubic, it is elastically isotropic; the chiral elastic aspect has not been evaluated. By using the analytical values obtained for the equivalent Young's modulus and Poisson's ratio E_x^* and ν_x^* one obtains a shear modulus G_1 = 1.85 MPa, which is 11% stiffer than the modulus predicted through biaxial shear. These differences between the homogenized shear modulus and the one calculated by assuming an isotropic linear elastic behavior of the lattice is however significantly lower than the one observed in structural chiral systems. Hexagonal and tetra-tessellated chiral lattices have equal uniaxial Young's moduli along the lattice coordinates and an in-plane Poisson's ratio close to -1 [11][26]. By using concepts of Poisson's ratio and Young's modulus, a continuum view of the material is implicitly assumed. If the structural elements are sufficiently small compared with the specimen, as is the case with common materials such as steel and aluminium, classical elasticity is the appropriate continuum approach in the linear regime. If the structural elements are sufficiently large, moments transmitted through them are of sufficient magnitude that they cannot be neglected. Cosserat or micropolar elasticity [47][48] is then an appropriate continuum elasticity theory that, in contrast to classical elasticity, contains a length scale. Cosserat solids such as foams [48] exhibit size effects in torsion and bending in which deformation gradients give rise to net moments. Simple tension or compression of normal cellular solids gives rise to moments in the ribs [49] that must be analysed, but these moments sum to zero in tension of such solids. Chiral 2D lattices [11] have been analysed [19][22][23][24] in the context of Cosserat elasticity. Chiral 3D solids exhibit stretch-twist coupling [52][53], but no such effects are observed in the present 2D solids.

From a structural integrity perspective, questions may arise from the use of a pattern with cuts and slits in a 2D material substrate. The edges of the cuts do create localized regions of stress concentration, and those would affect the overall structural performance and deformation behaviour of the chiral hinge lattice. Although the current work is concerned with the in-plane homogenized linear elastic constants of this lattice, it is worth discussing some consideration about the impact provided by the presence of the slits. Within the PMMA samples fabricated in this work, brittle failure was indeed observed, with cracks originated at the corners of the slits and roots of the ribs. Although the lattice is very compliant, the use of a brittle substrate would limit the elastic range of deformations, and in that case the use of an elastomeric substrate would be advisable, as adopted in other perforated metamaterials [28][30]. The use of a metal substrate with an elasto-plastic mechanical behaviour would lead to the formation of plastic regions in the corners of the cuts prior to failure. The localized plastic regions would create equivalent plastic hinges, and therefore increase the coupling between uniaxial deformation and in-plane rotation during the loading. Further mechanical tailoring could involve the rounding of the corners to ameliorate the stress concentration. In any case, the efficient engineering use of this

lattice topology would involve a careful selection of the substrate material, as well as the manufacturing technology to control the dimensions and features of the slits patterns.

6. Conclusions

In this work, a novel chiral hinge lattice with a marginal in-plane negative Poisson's ratio is designed, modeled and experimentally evaluated. The square lattice has been produced by rotationally symmetric patterns of slits. The theoretical and numerical models show good agreement with the experimental data. For large slits to ribs aspect ratios of the unit cell, the bending and axial deformations provide the main contribution to the elasticity of the lattice. The Poisson's ratio of the core material has a negligible effect on the homogenized stiffness and equivalent Poisson's ratio of the lattice. The chiral hinge lattice shows a very high compliance compared to other structures defined by patterns of slits, and a high in-plane shear stiffness with a quasi-isotropic behaviour compared to other structural chiral configurations.

Acknowledgements

WZ and DZ would like to thank the China National Science Foundation for their fellowship. RN also acknowledges the support from UK Engineering and Physical Sciences Research Council (EPSRC) for his Postdoctoral Fellowship. FS would like to thank the European Commission for the computational and testing logistics provided through the H2020 MSC ITN VIPER project.

References

[1] J.H. Lee, J.P. Singer, and E.L. Thomas, Micro- /Nanostructured Mechanical Metamaterials, Adv. Mater. 24, 4782 (2012)

[2] J. Christensen, M. Kadic, O. Kraft, and M. Wegener, Vibrant times for mechanical metamaterials, MRS Communications 5, 453 (2015)

[3] T. Frenzel, C. Findeisen, M. Kadic, P. Gumbsch, and M. Wegener, Tailored Buckling Microlattices as Reusable Light- Weight Shock Absorbers, Adv. Mater. (2016).

[4] S.H. Kang, S. Shan, W.L. Noorduin, M. Khan, J. Aizenberg, and K. Bertoldi, Buckling- Induced Reversible Symmetry Breaking and Amplification of Chirality Using Supported Cellular Structures, Adv. Mater. 25, 3380 (2013).

[5] A.S. Phani, J. Woodhouse, and N. Fleck, Wave propagation in two-dimensional periodic lattices, The Journal of the Acoustical Society of America 119, 1995 (2006).

[6] Y. Tang, G. Lin, L. Han, S. Qiu, S. Yang, and J. Yin, Design of hierarchically cut hinges for highly stretchable and reconfigurable metamaterials with enhanced strength, Adv. Mater. 27, 7181 (2015).

[7] R. Lakes, Foam structures with a negative Poisson's ratio, Science 235, 1038 (1987).

[8] K.E. Evans, M.A. Nkansah, I.J. Hutchinson, S.C. Rogers, Nature 353 (1991) 124.

[9] H. Yasuda and J. Yang, Reentrant Origami-Based Metamaterials with Negative Poisson's Ratio and Bistability, Phys. Rev. Lett. 114, 185502 (2015).

[10] Wojciechowski KW. Two-dimensional isotropic systems with a negative Poisson ratio. Phys Lett 1989; A137:60–4.

[11] Prall D, Lakes R. Properties of a chiral honeycomb with Poisson's ratio -1. Int J Mech Sci 1996; 39: 305–14.

[12] Lorato A, Innocenti P, Scarpa F, Alderson A, Alderson KL, Zied KM, et al. The transverse elastic properties of chiral honeycombs. Compos Sci Technol 2010; 70: 1057-63.

[13] Spadoni A, Ruzzene M, Scarpa F. Global and local linear buckling behaviour of a chiral cellular structure. Phys Status Solidi (b) 2005;242(3): 695–709.

[14] F. Scarpa, S. Blain, T. Lew et al. Elastic buckling of hexagonal chiral cell honeycombs. Composites: Part A 38 (2007) 280–289

[15] M.R. Hassan, F. Scarpa, M. Ruzzene, N.A. Mohammedd. Smart shape memory alloy chiral honeycomb. Materials Science and Engineering A 481–482 (2008) 654–657.

[16] Grima JN, Gatt R, Farrugia PS (2008b). On the properties of auxetic meta-tetrachiral structures. Phys. Stat. Sol., 245: 511-520.

[17] W. Miller, C.W. Smith, F. Scarpa, K.E. Evans. Flatwise buckling optimization of hexachiral and tetrachiral honeycombs. Composites Science and Technology 70 (2010) 1049–1056

[18] A. Alderson et al, Elastic constants of 3-, 4- and 6-connected chiral and anti-chiral honeycombs subject to uniaxial in-plane loading. Composites Science and Technology 70 (2010) 1042–1048

[19] A. Spadoni, M. Ruzzene, Elasto-static micropolar behavior of a chiral auxetic lattice, J. Mech. Phys. Solids 60 (2012) 156–171.

[20] X.N. Liu, G.L. Huang, G.K. Hua. Chiral effect in plane isotropic micropolar elasticity and its application to chiral lattices. Journal of the Mechanics and Physics of Solids 60 (2012) 1907–1921.

[21] Chen YJ, Scarpa F, Liu YJ, Leng JS. Elasticity of anti-tetrachiral anisotropic lattices. Int J Solids Struct 2013;50(6):996-1004.

[22] Y. Chen, X. Liu, G. Hu, Micropolar modeling of planar orthotropic rectangular chiral lattices, Comptes Rendus Mécanique 342 (2014) 273–283.

[23] Y. Chen, X. Liu, G. Hu, et al., Micropolar continuum modelling of bi-dimensional tetrachiral lattices, Proc. R. Soc. A 470 (2014) 20130734.

[24] A. Bacigalupo, L. Gambarotta, Homogenization of periodic hexa-and tetrachiral cellular solids, Compos. Struct. 116 (2014) 461–476.

[25] D Mousanezhad et al. Elastic properties of chiral, anti-chiral, and hierarchical honeycombs: A simple energy-based approach. Theoretical and Applied Mechanics Letters 6 (2016) 81–96

[26] A. Alderson et al. The in-plane linear elastic constants and out-of-plane bending of 3-coordinated ligament and cylinder-ligament honeycombs. Composites Science and Technology 70 (2010) 1034–1041

[27] Liu X. N., Hu G. K., Sun C. T. and Huang G. L. Wave propagation characterization and design of two-dimensional elastic chiral metacomposite. Journal of Vibration and Sound 330 (2011), 2536-2553.

[28] Bertoldi K, Reis PM, Willshaw S, Mullin T. Negative Poisson's ratio behavior induced by an elastic instability. Advanced Materials. 2010;22 :361-366.

[29] J N. Grima, R Gatt. Perforated Sheets Exhibiting Negative Poisson's Ratios. Advanced Engineering

Materials. 2010, 12, 460-464.

[30] Cho Y, Shin J-H, Costa A, Kim TA, Kunin V, Li J, et al. Engineering the shape and structure of materials by fractal cut. Proc Natl Acad Sci 2014;111 (49):17390–5.

[31] R. Gatt et al. Hierarchical Auxetic Mechanical Metamaterials. Sci. Rep. 2015, 5, 8395.

[32] A Rafsanjani, D Pasini. Bistable auxetic mechanical metamaterials inspired by ancient geometric motifs. Extreme Mechanics Letters 9 (2016) 291–296.

[33] A. Slann, W. White, F. Scarpa, K. Boba, I. Farrow. Cellular plates with auxetic rectangular perforations. Phys. Stat. Sol. B. 2015, 252, 1533.

[34] M. Taylor, L Francesconi, et al. Low Porosity Metallic Periodic Structures with Negative Poisson's Ratio. Adv. Mater. 26, 2365 (2014).

[35] L Mizzi et al. Auxetic metamaterials exhibiting giant negative Poisson's ratios. Phys. Status Solidi RRL 9, No. 7, 425–430 (2015)

[36] Billon K et al. Mechanics and band gaps in hierarchical auxetic rectangular perforated composite metamaterials. Composite Structures 160 (2017) 1042–1050.

[37] J N. Grima, L Mizzi, K M. Azzopardi, R Gatt. Auxetic Perforated Mechanical Metamaterials with Randomly Oriented Cuts. Adv. Mater. 28 (2016), 385–389

[38] P Bettini, A Airoldi, G Sala, L Di Landro, M Ruzzene, A Spadoni. Composite chiral structures for morphing airfoil: Numerical analyses and development of a manufacturing process. Composites: Part B Engineering, 41 (2010), 133-147.

[39] G Cicala, G Recca, L Oliveri, Y Perikleous, F Scarpa, C Lira, A Lorato, DJ Grube, G Ziegmann. Hexachiral truss-core with twisted hemp yarns: Out-of-plane shear properties. Composite Structures 94 (2012), 3556-3562

[40] Peano, G. Sur une courbe, qui remplit toute une aire plane. Mathematische Annalen, 36(1) (1890) 157–160

[41] F. Dos Reis, J.F. Ganghoffer. Equivalent mechanical properties of auxetic lattices from discrete homogenization. Composite Structures 51 (2012), 314-321

[42] Cowper GR. The shear coefficient in Timoshenko's beam theory. J Appl Mech 1966;33(2):335e40.

[43] V Salit, T Weller. On the feasibility of introducing auxetic behavior into thin-walled structures. Acta Materialia 57 (2009) 125–135.

[44] Kohnme P. ANSYS help documentation. ANSYS, Inc. Theory Release. 2003;8.

[45] Mohammad Sanami, Naveen Ravirala, Kim Alderson, Andrew Alderson. Auxetic Materials for Sports Applications. Procedia Engineering, 72, 2014, Pages 453-458.

[46] Huang J, Gong X, Zhang Q, Scarpa F, Liu Y, Leng J. In-plane mechanics of a novel zero Poisson's ratio honeycomb core. Compos Part B Eng 2016;89: 6776.

[47] E. Cosserat, and F. Cosserat. *Theorie des Corps Deformables*, Hermann et Fils, Paris (1909).

[48] A.C. Eringen. Theory of micropolar elasticity. In *Fracture* Vol. 1, 621-729 (edited by H. Liebowitz), Academic Press (1968).

[49] Rueger, Z. and Lakes, R. S. Experimental Cosserat elasticity in open cell polymer foam. Philosophical

Magazine 96(2) (2016), 93-111.

[50] L. J. Gibson, M. F. Ashby, G. S. Schajer, and C. I. Robertson. The mechanics of two dimensional cellular solids. Proc. Royal Society London, A382 (1982), 25-42.

[51] R. Zhu, X. N. Liu, G. K. Hu, C. T. Sun and G. L. Huang. Negative refraction of elastic waves at the deep-subwavelength scale in a single-phase metamaterial. Nature Communications, (2014) 5(5):5510.

[52] R. S. Lakes and R. L. Benedict. Noncentrosymmetry in micropolar elasticity. International Journal of Engineering Science 29(10) (1982) 1161-1167.

[53] Ha, C. S., Plesha, M. E., Lakes, R. S. Chiral three-dimensional isotropic lattices with negative Poisson's ratio. Physica Status Solidi B, 253(7) (2016), 1243-1251.

[54] Gaspar N, Smith CW, Alderson A, Grima JN, Evans KE. A generalised threedimensional tethered-nodule model for auxetic materials. Journal of Materials Science 46(2) (2011), 372-384

Figures Captions

Fig.1 (a) Chiral hinge lattice panels made out of laminate wood. (b) Geometry of chiral hinge unit cell

Fig.2 Schematic illustration of theoretical modelling of the unit cell (a=6b): (a) element division; (b) structure simplification; (c) statically determinate structure with complementary conditions

Fig. 3. Typical shear-test fixtures (Fig. 5 of Ref. [43])

Fig.4 Schematic illustration of theoretical model for the chiral unit cell (a=10b) under biaxial shear modelling: (a) elements division; (b) statically determinate structure with complementary conditions

Fig.5 Boundary conditions for (a) the tensile and (b) the biaxial shear loading.

Fig.6 FE models used for the convergence test. (a) 1/4 Model A; (b) 1/4 Model B; (c) 1/4 Model C; (d) 1/4 Model D

Fig.7 Effect of the cells number on the convergence.

Fig.8 Specimen for (a) tensile and (b) off-axis 45o shear tests.

Fig. 9. Experimental data processing for effective Poisson's ratio (a) Transverse vs. longitudinal strains (b) fitting curves

Fig.10. Effective Poisson's ratio vs the longitudinal strain with corresponding standard deviation

Fig. 11 Three types of RUC with different aspect ratios of slit to ribs: (a) a/b=6, (b) a/b=10, (c) a/b=14

Fig. 12 Comparisons between the analytical and FEA results for different slit/ribs length ratios: (a) non-dimensional effective Young's modulus, (b) non-dimensional effective shear modulus, (c) Poisson's ratio. B, A, S mean Bending, Axial and Shear deformations, respectively.

Tables

Table 1 Comparison for the models and results

Model	Overall element size (mm)	Refinement at corners	Total DOFs for one cell	E^*_x		v^*_x	
				Absolute value (MPa)	Relative value	Absolute value	Relative value
A	0.3	No	27,704	3.2179	1.0086	-0.02129	0.9387
B	**0.3**	**Yes**	**43,806**	**3.1975**	**1.0023**	**-0.02327**	**1.0260**
C	0.1	No	224,304	3.1975	1.0023	-0.02145	0.9458
D	0.1	Yes	242,648	3.1903	1.0000	-0.02268	1.0000

Table 2. Comparisons of the homogenized in-plane engineering constants from the analytical, numerical and experimental.

	Effective elastic modulus E^*_x (MPa)	Poisson's ratio v^*_x	Effective Shear modulus G^*_x (MPa)
Analytical	3.55	-0.041	1.64
FEM	3.26	-0.039	1.70
Experimental	3.49±0.15	-0.038±0.01	1.79±0.11

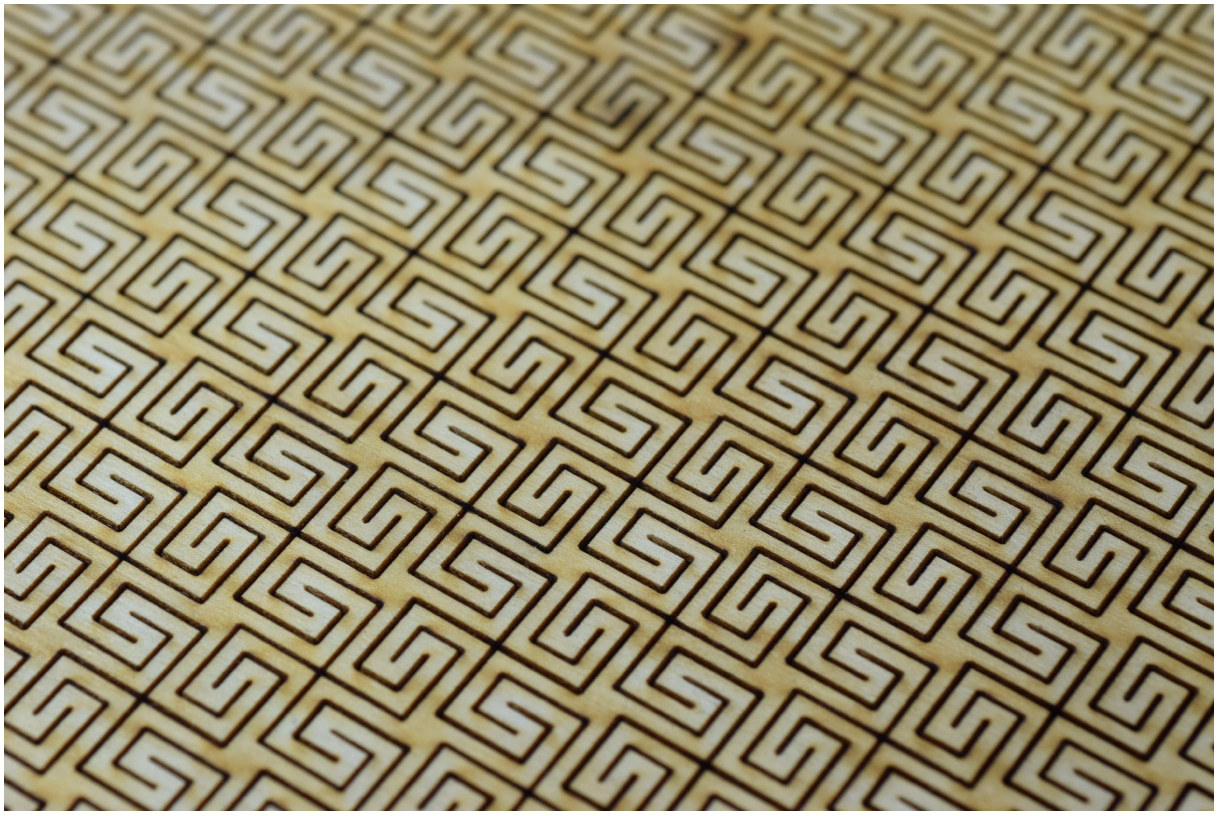

Fig. 1a

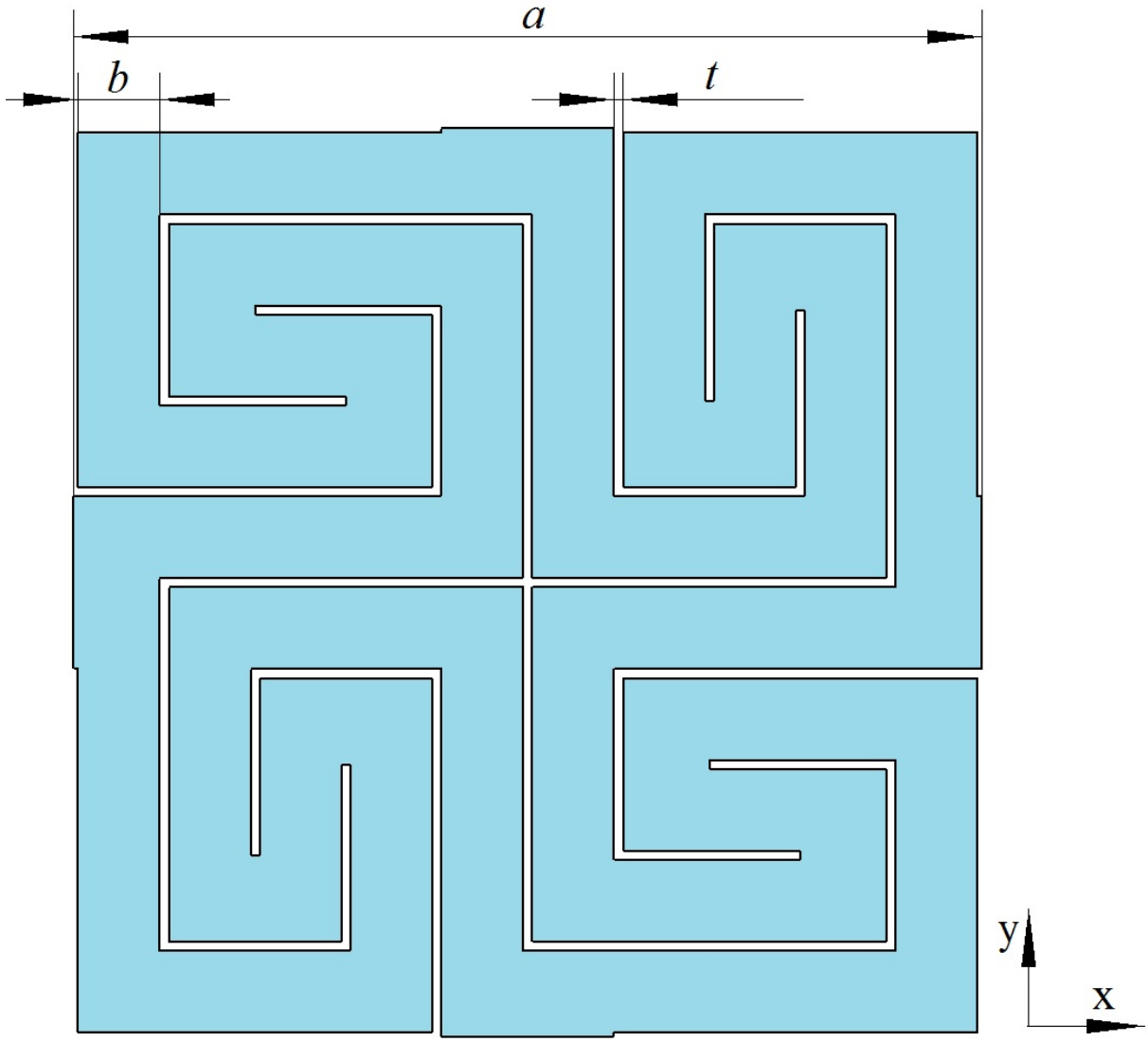

Fig. 1b

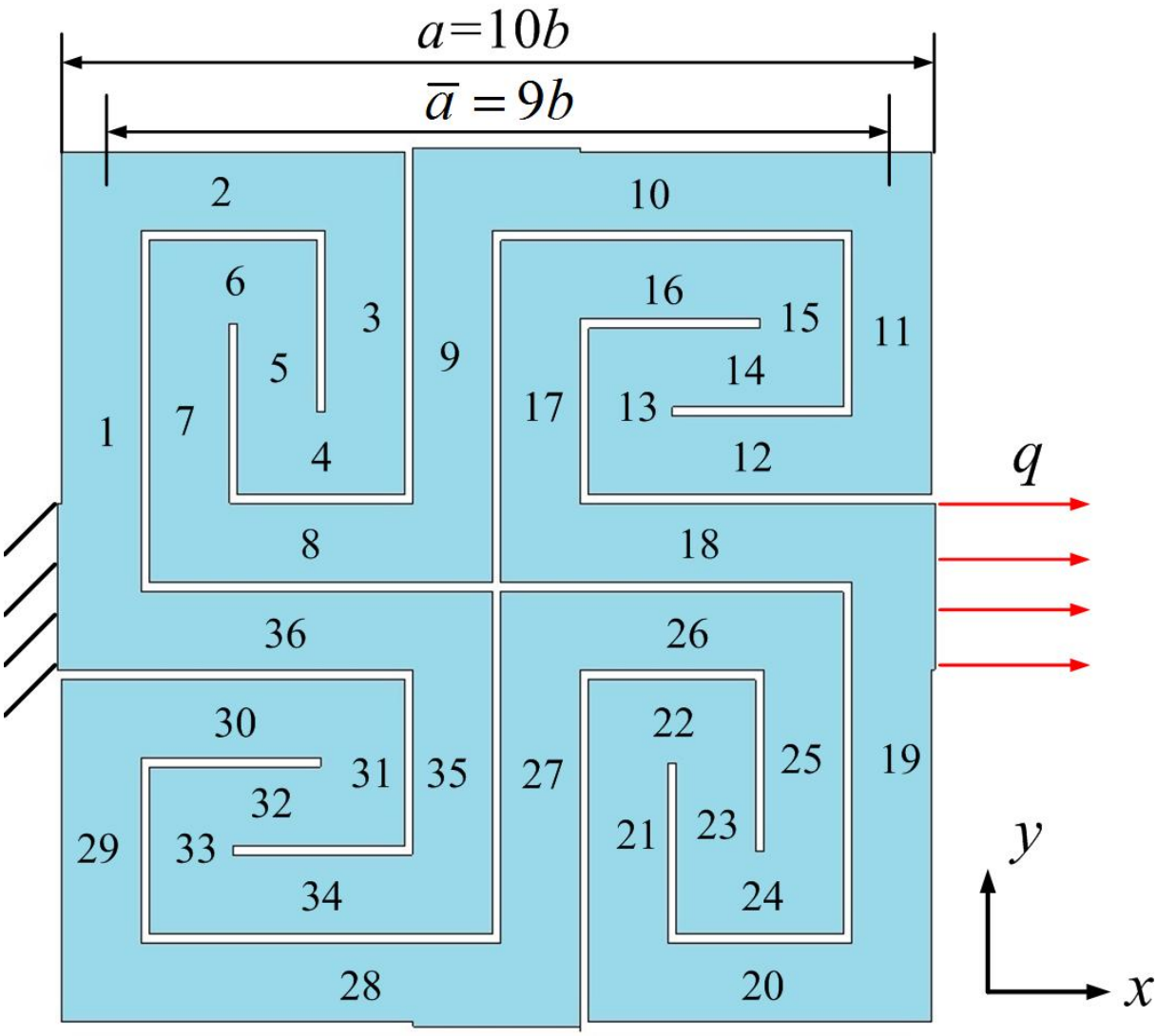
a=10b
ā = 9b
2
10
6
3
16
15
11
5
9
14
1
7
17
13
4
12
q
8
18
36
26
30
22
31
35
25
19
32
27
29
33
21
23
34
24
28
20
y
x

Fig. 2a

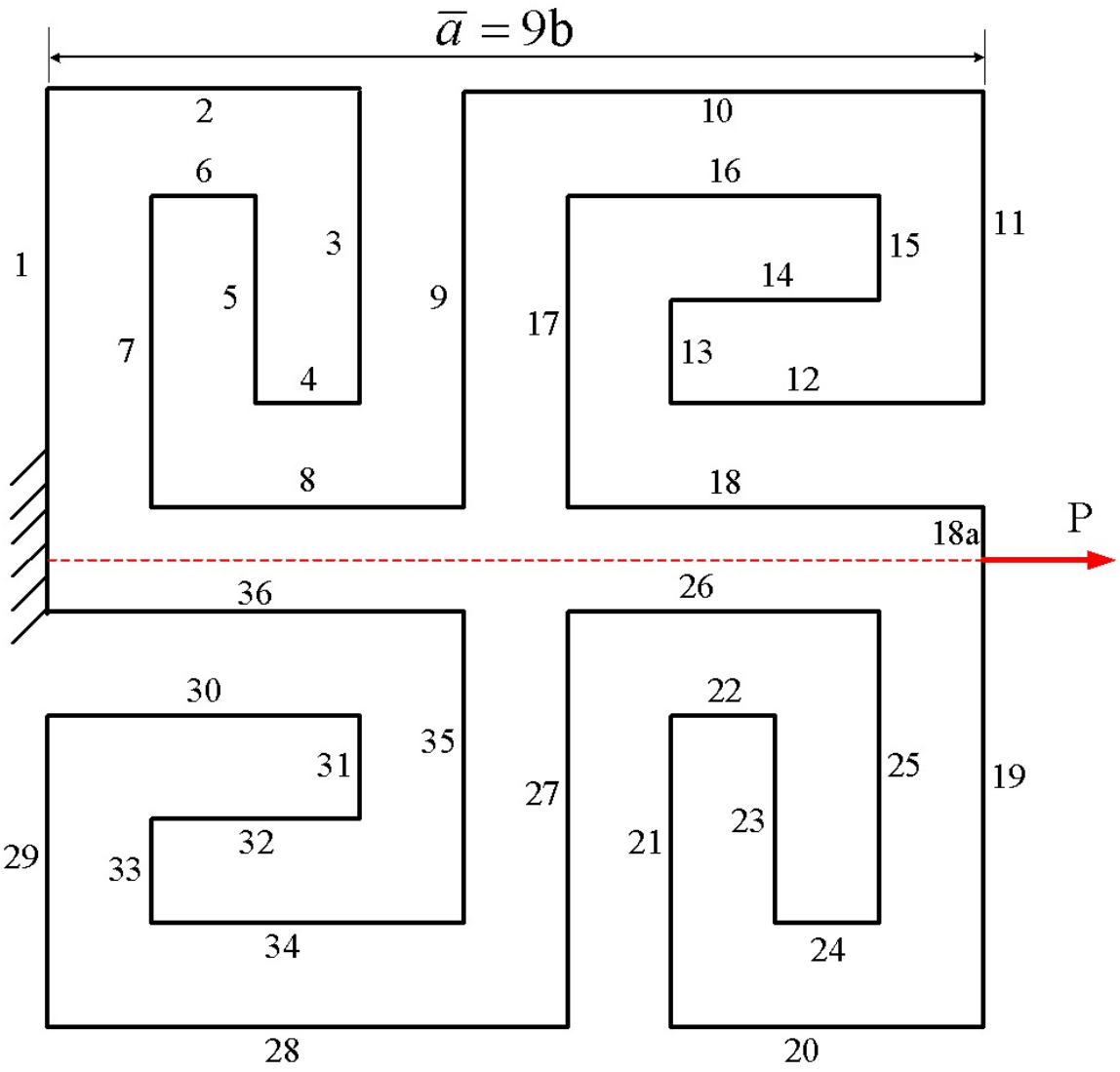
$\bar{a} = 9b$
1
2
3
4
5
6
7
8
9
10
11
12
13
14
15
16
17
18
18a
P
19
20
21
22
23
24
25
26
27
28
29
30
31
32
33
34
35
36

Fig. 2b

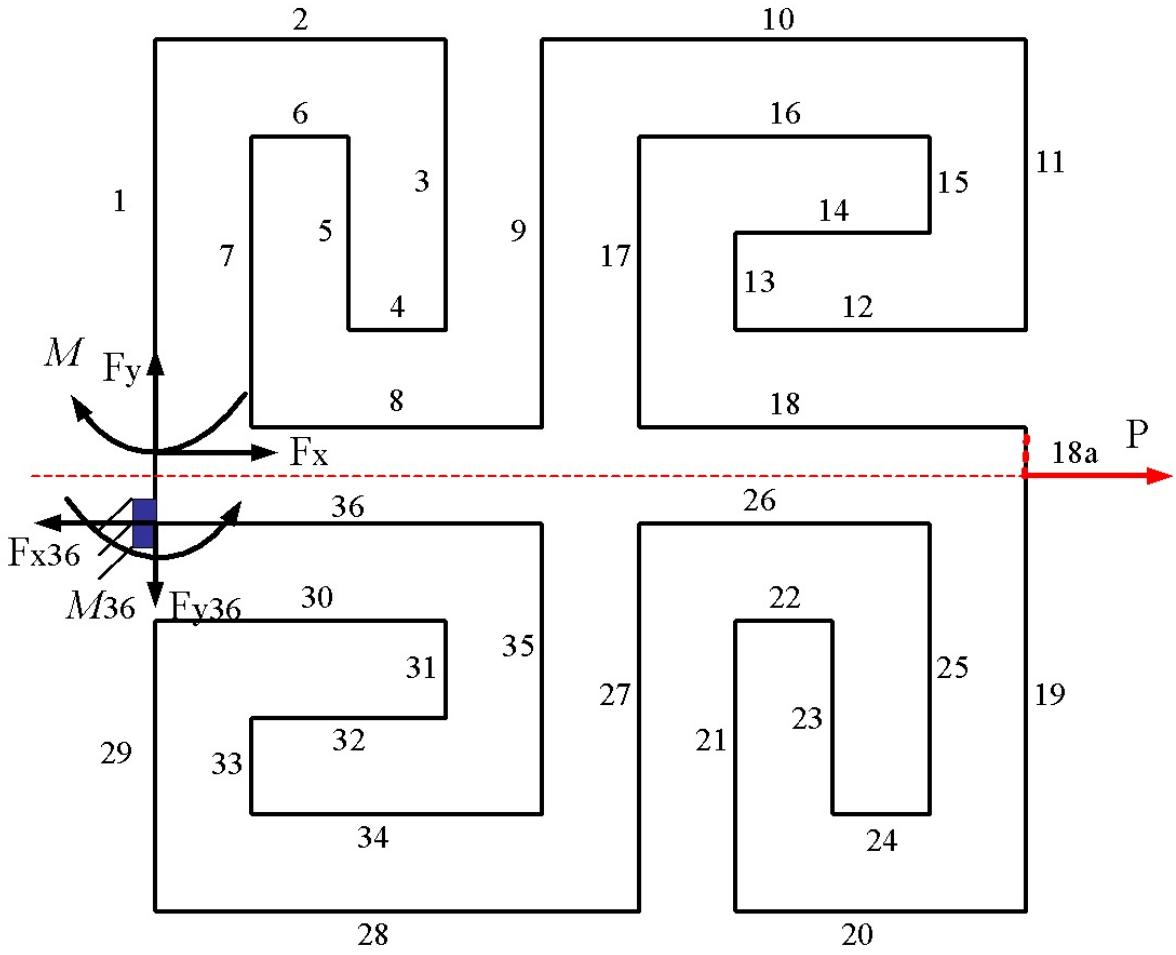
2
10
6
16
1
3
11
15
5
14
9
7
17
13
4
12
M
Fy
8
18
P
Fx
18a
36
26
Fx36
M36
Fy36
30
22
35
31
25
27
23
19
29
21
32
33
34
24
28
20

Fig. 2c

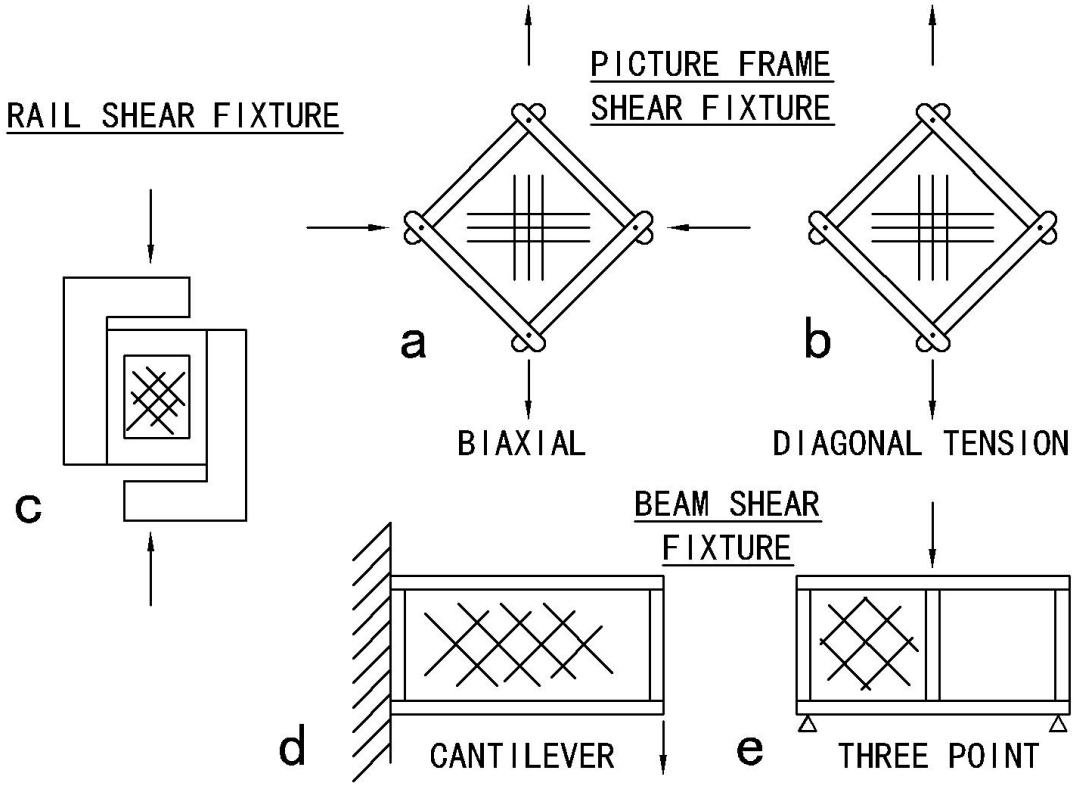
RAIL SHEAR FIXTURE
PICTURE FRAME
SHEAR FIXTURE
a
b
c
BIAXIAL
DIAGONAL TENSION
BEAM SHEAR
FIXTURE
d
CANTILEVER
e
THREE POINT

Fig. 3

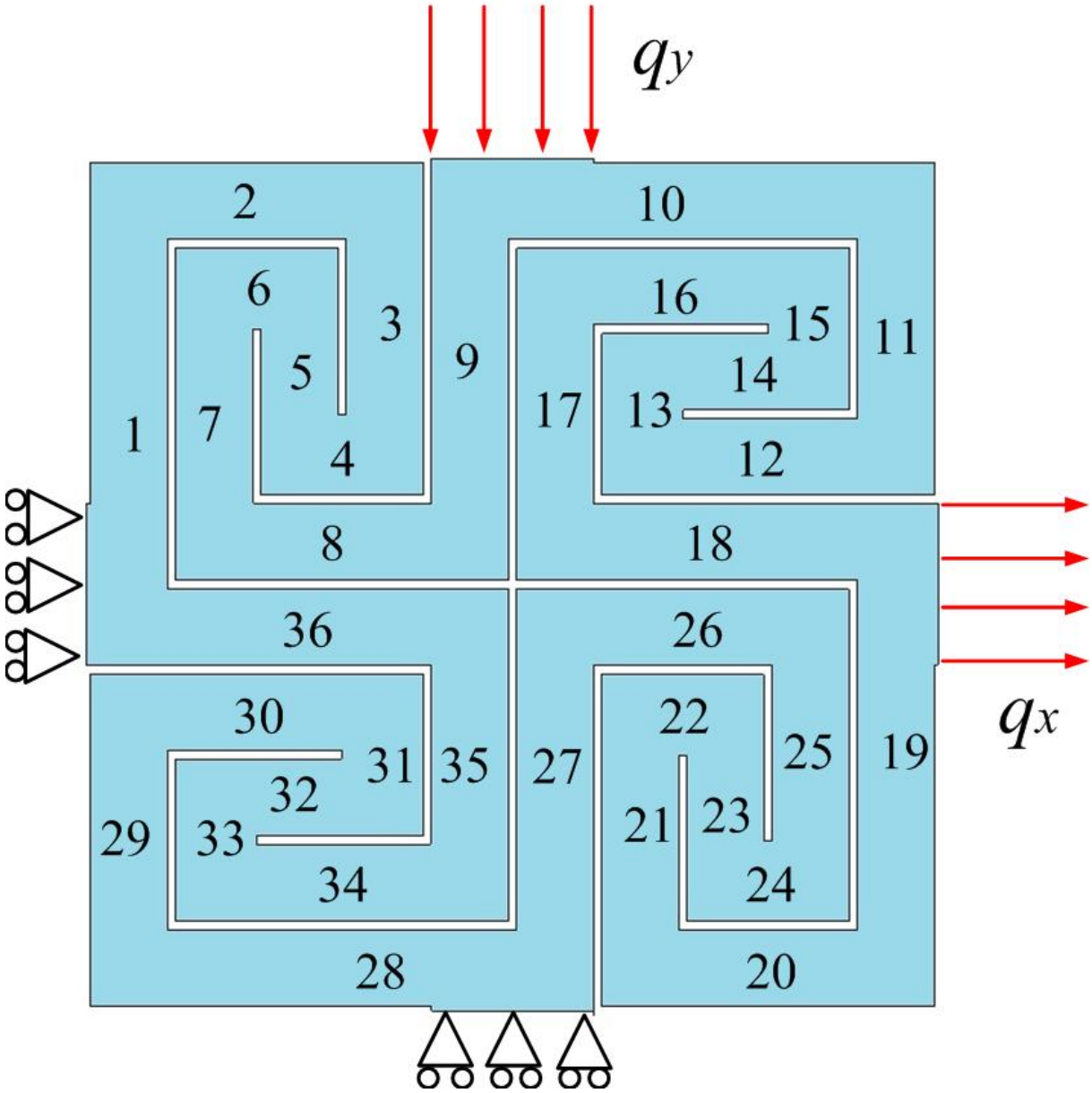
qy
2
10
6
16
3
15
11
5
9
14
1
7
17
13
4
12
8
18
36
26
30
22
31
35
25
19
32
27
29
33
21
23
34
24
28
20
qx

Fig. 4a

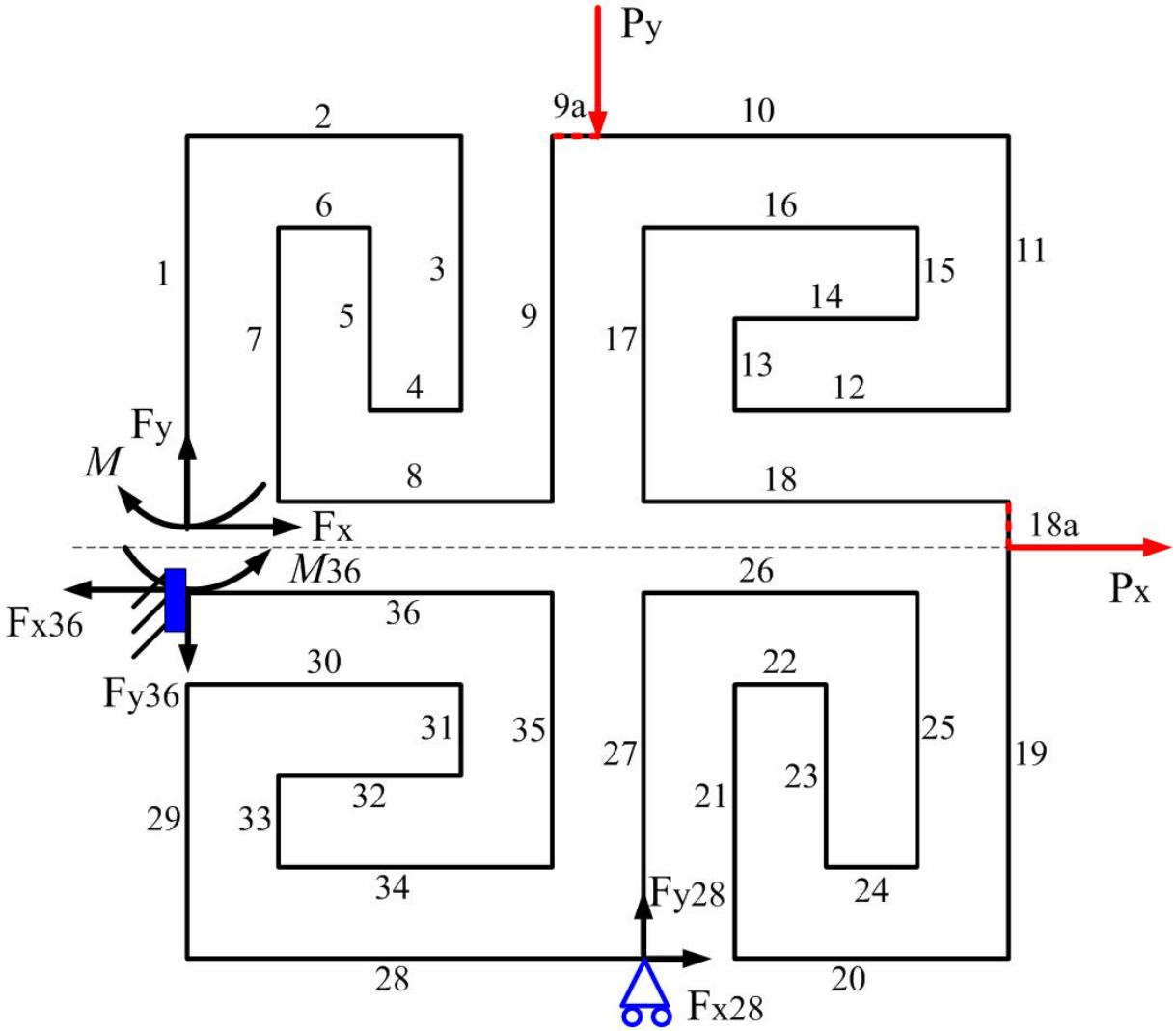
Py
9a
2
10
6
16
1
3
11
15
5
14
7
9
17
13
4
12
Fy
M
8
18
Fx
18a
M36
Px
26
Fx36
36
30
22
Fy36
31
35
25
27
19
23
32
21
29
33
24
34
Fy28
28
20
Fx28

Fig. 4b

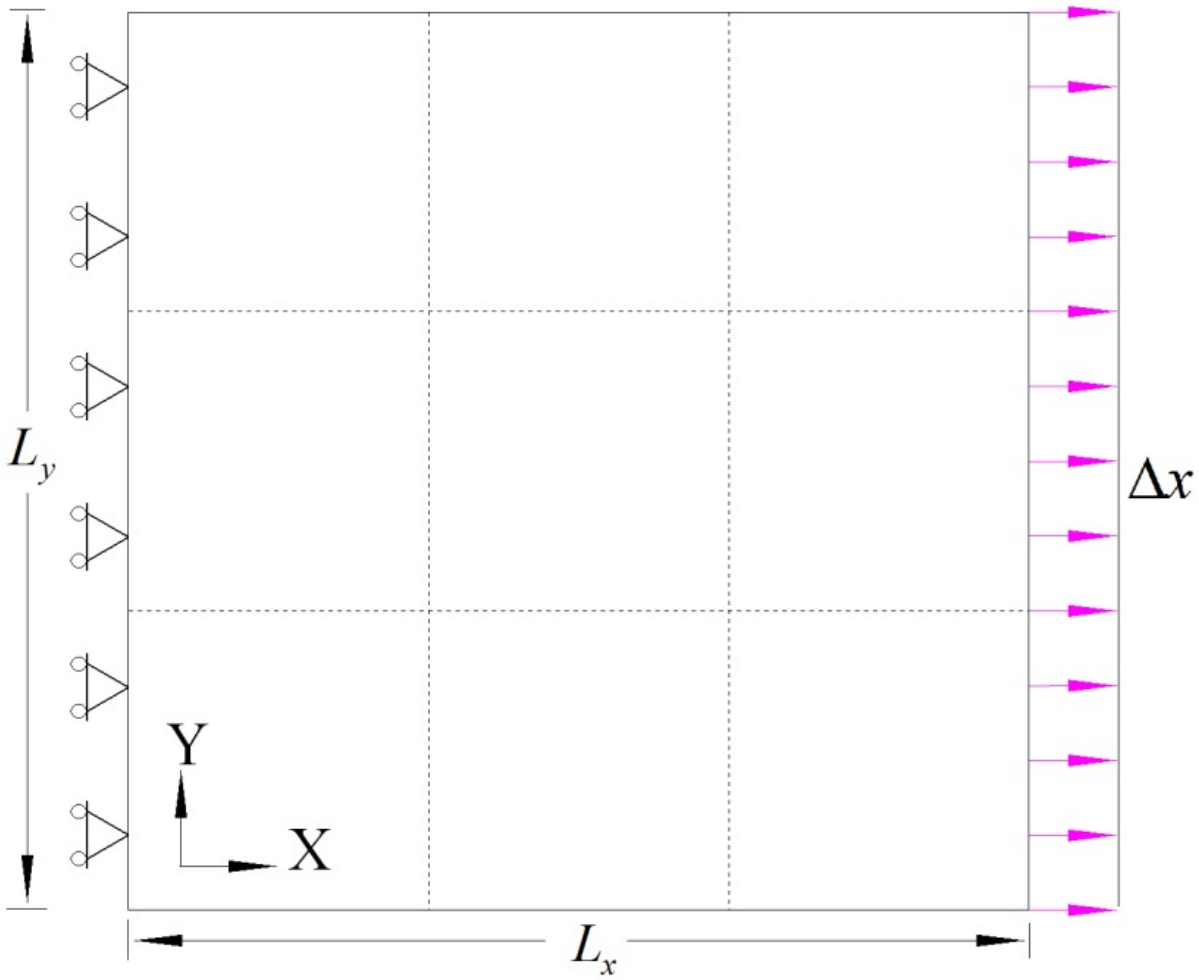

Fig. 5a

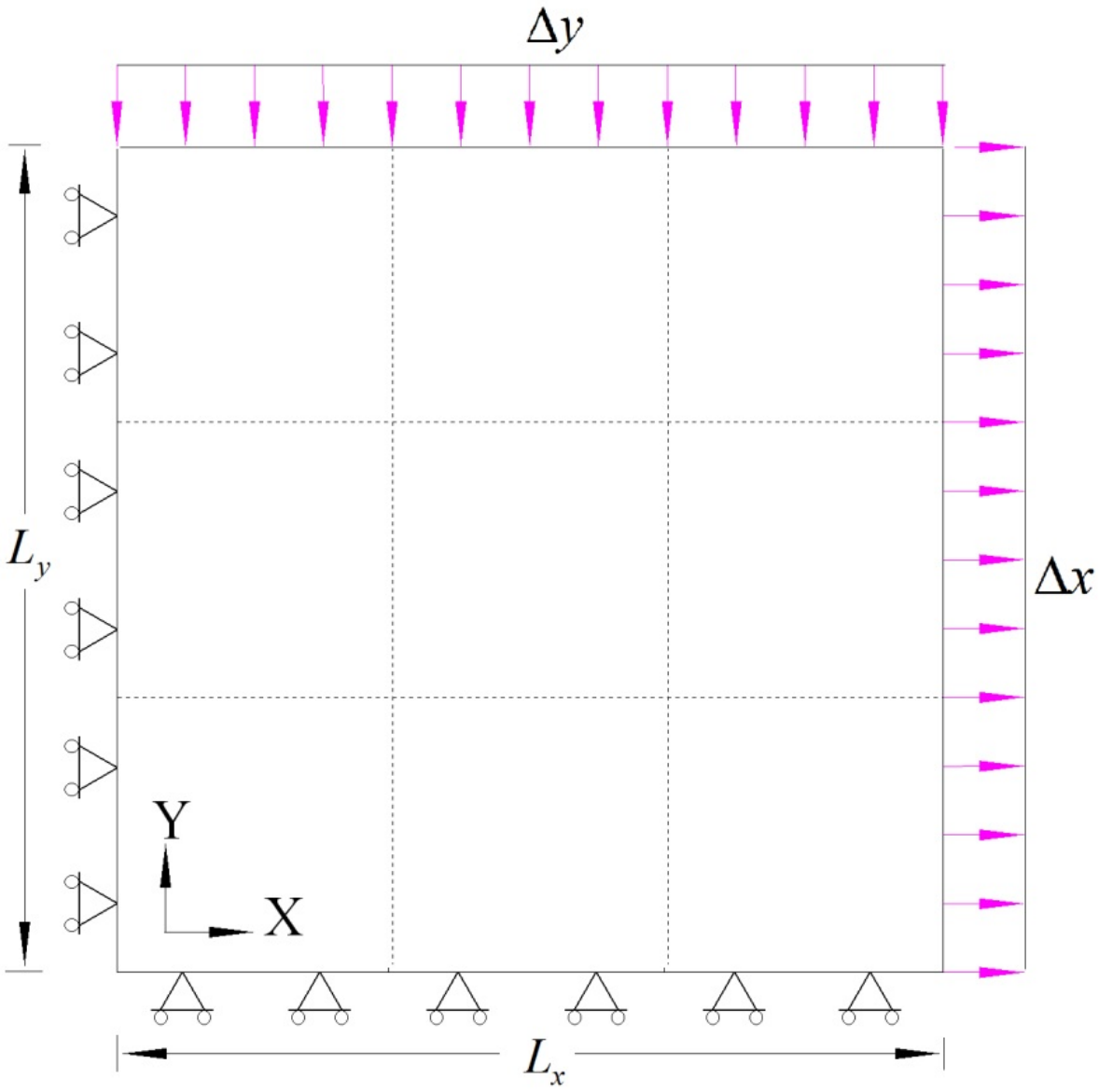

Fig. 5b

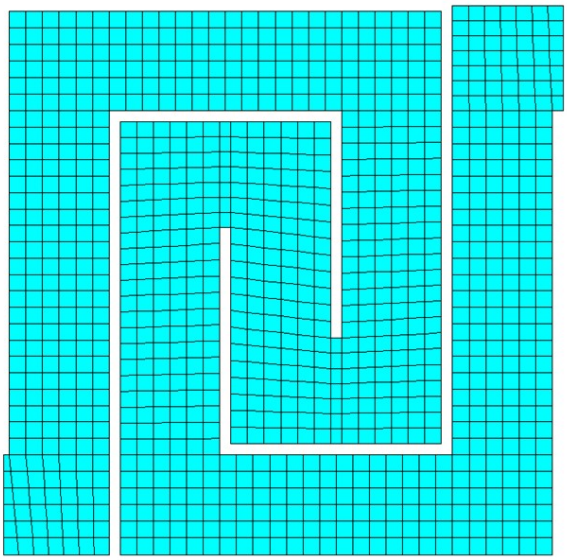

Fig. 6a

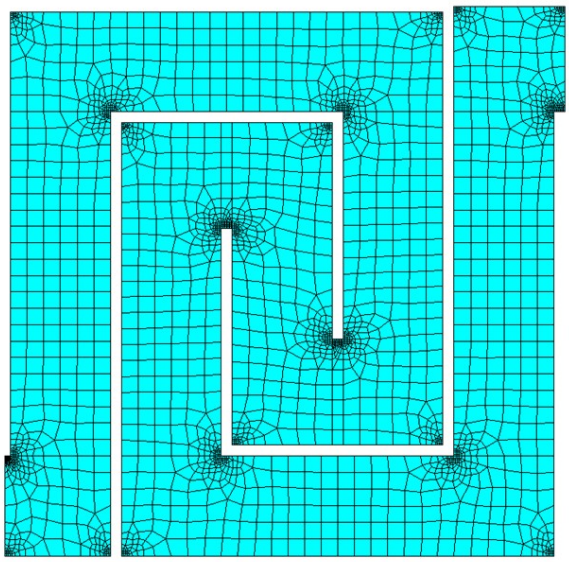

Fig. 6b

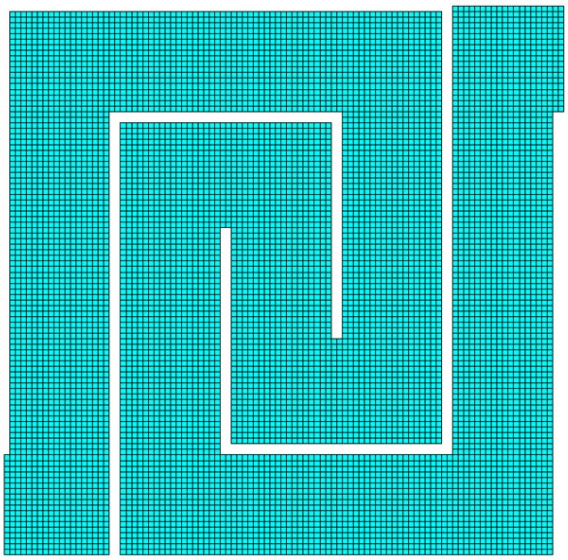

Fig. 6c

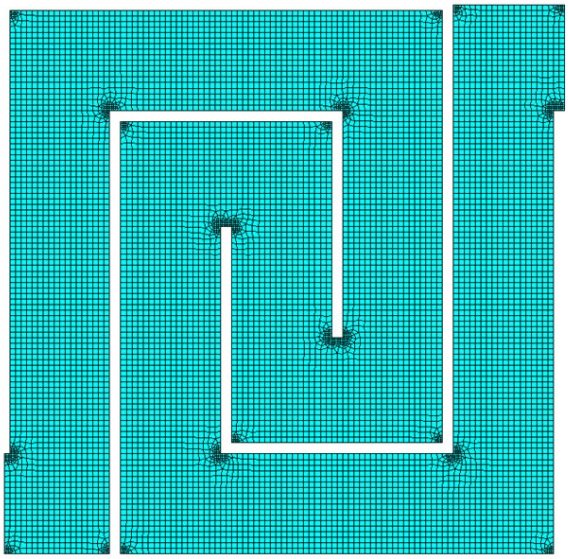

Fig. 6d

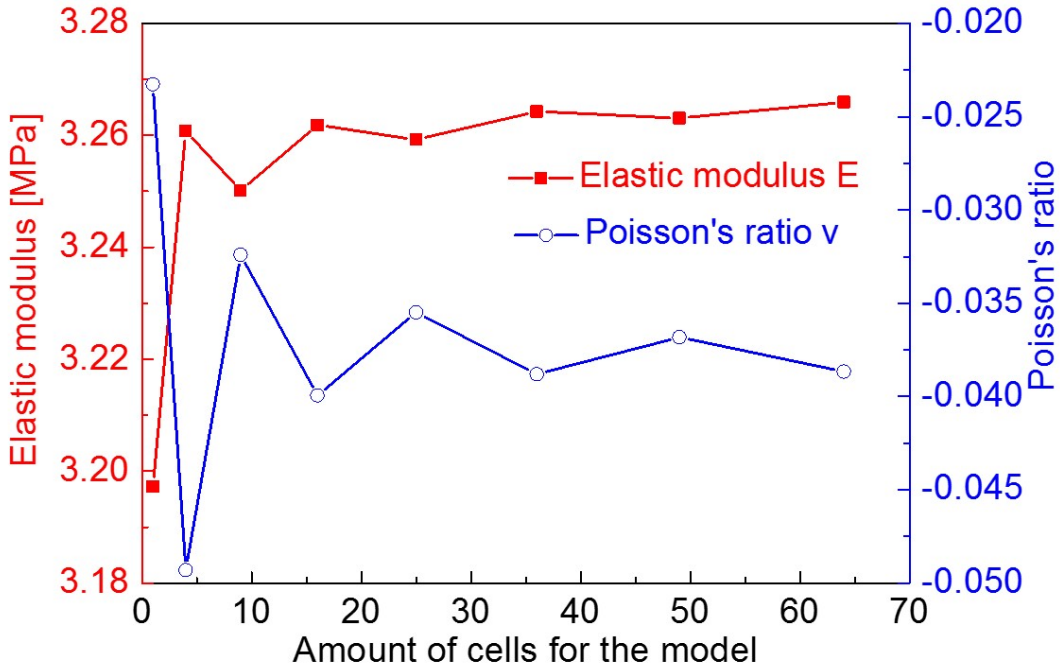
3.28
3.26
3.24
3.22
3.20
3.18
Elastic modulus [MPa]
-0.020
-0.025
-0.030
-0.035
-0.040
-0.045
-0.050
Poisson's ratio
Elastic modulus E
Poisson's ratio v
0
10
20
30
40
50
60
70
Amount of cells for the model

Fig. 7

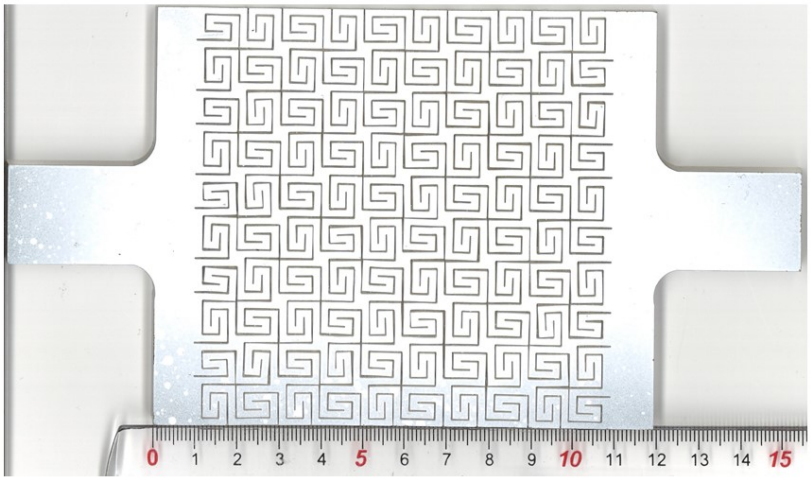
0 1 2 3 4 5 6 7 8 9 10 11 12 13 14 15

Fig. 8a

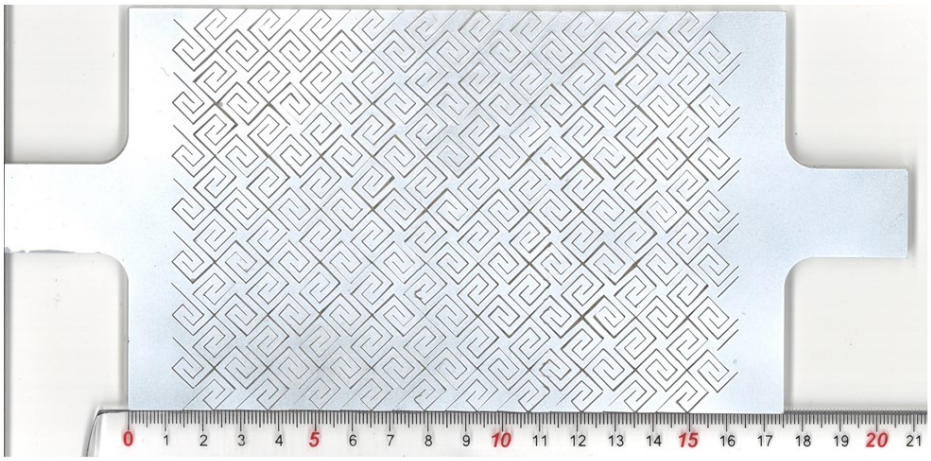

Fig. 8b

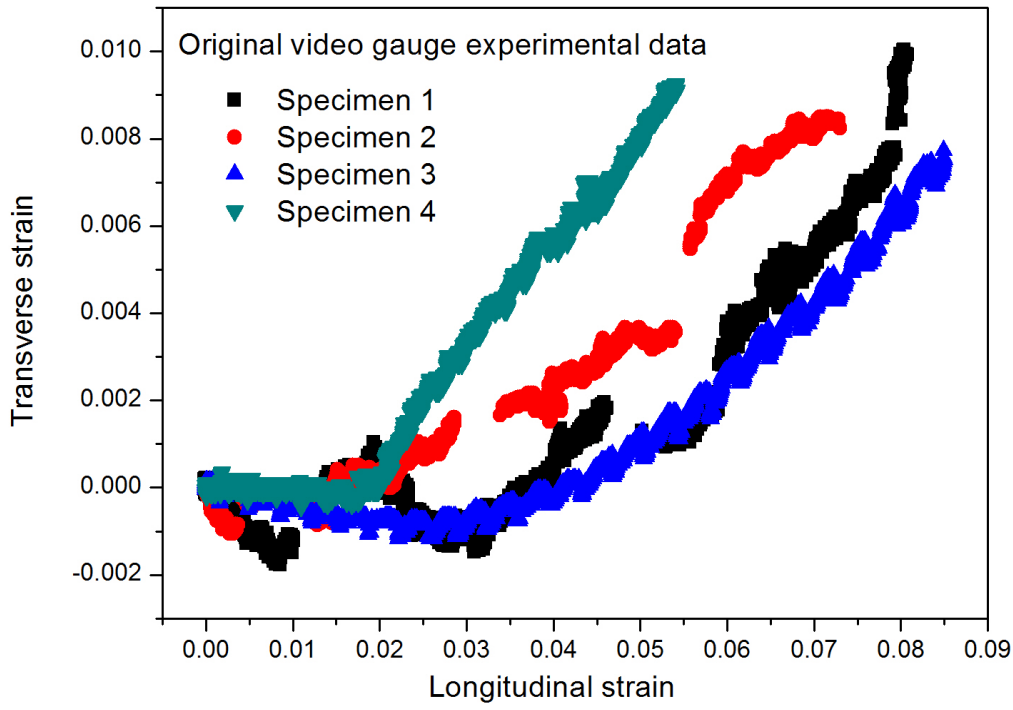
Original video gauge experimental data
Specimen 1
Specimen 2
Specimen 3
Specimen 4
Transverse strain
Longitudinal strain
0.010
0.008
0.006
0.004
0.002
0.000
-0.002
0.00
0.01
0.02
0.03
0.04
0.05
0.06
0.07
0.08
0.09

Fig. 9a

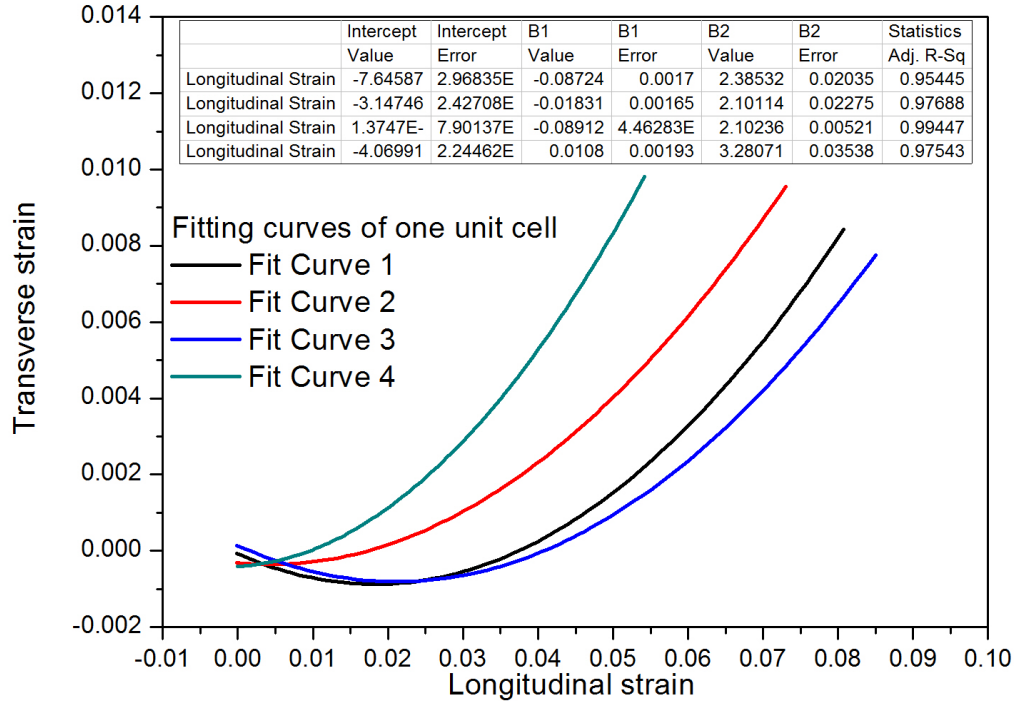
Intercept Intercept B1 B1 B2 B2 Statistics
Value Error Value Error Value Error Adj. R-Sq
Longitudinal Strain -7.64587 2.96835E -0.08724 0.0017 2.38532 0.02035 0.95445
Longitudinal Strain -3.14746 2.42708E -0.01831 0.00165 2.10114 0.02275 0.97688
Longitudinal Strain 1.3747E- 7.90137E -0.08912 4.46283E 2.10236 0.00521 0.99447
Longitudinal Strain -4.06991 2.24462E 0.0108 0.00193 3.28071 0.03538 0.97543
Fitting curves of one unit cell
Fit Curve 1
Fit Curve 2
Fit Curve 3
Fit Curve 4
Transverse strain
Longitudinal strain
0.014
0.012
0.010
0.008
0.006
0.004
0.002
0.000
-0.002
-0.01 0.00 0.01 0.02 0.03 0.04 0.05 0.06 0.07 0.08 0.09 0.10

Fig. 9b

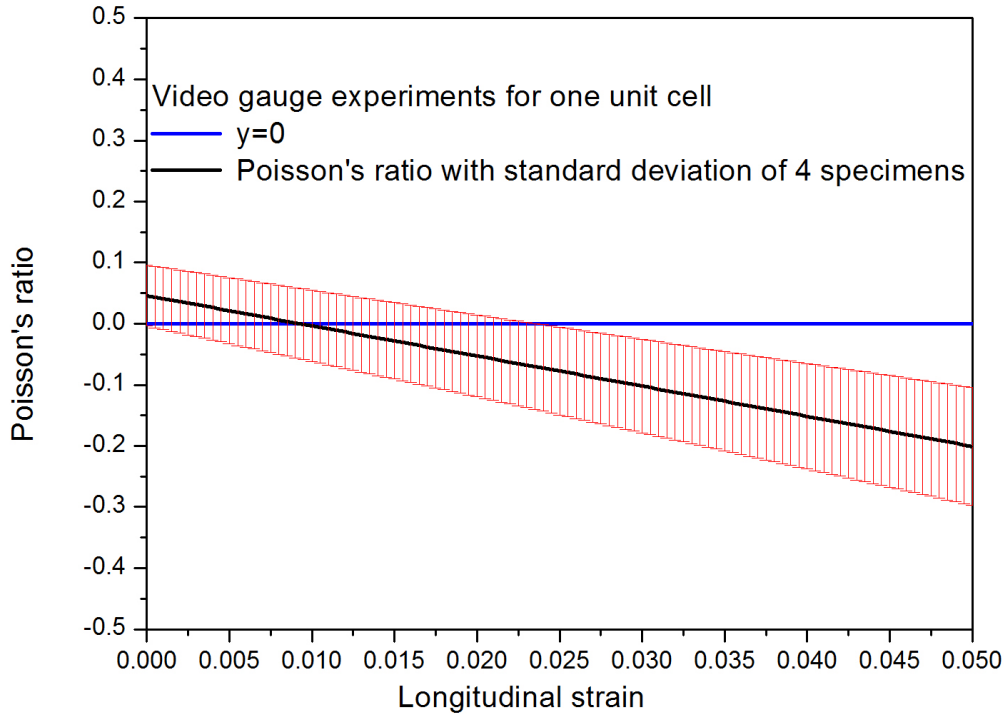
Video gauge experiments for one unit cell
y=0
Poisson's ratio with standard deviation of 4 specimens
Poisson's ratio
Longitudinal strain
0.5
0.4
0.3
0.2
0.1
0.0
-0.1
-0.2
-0.3
-0.4
-0.5
0.000 0.005 0.010 0.015 0.020 0.025 0.030 0.035 0.040 0.045 0.050

Fig. 10

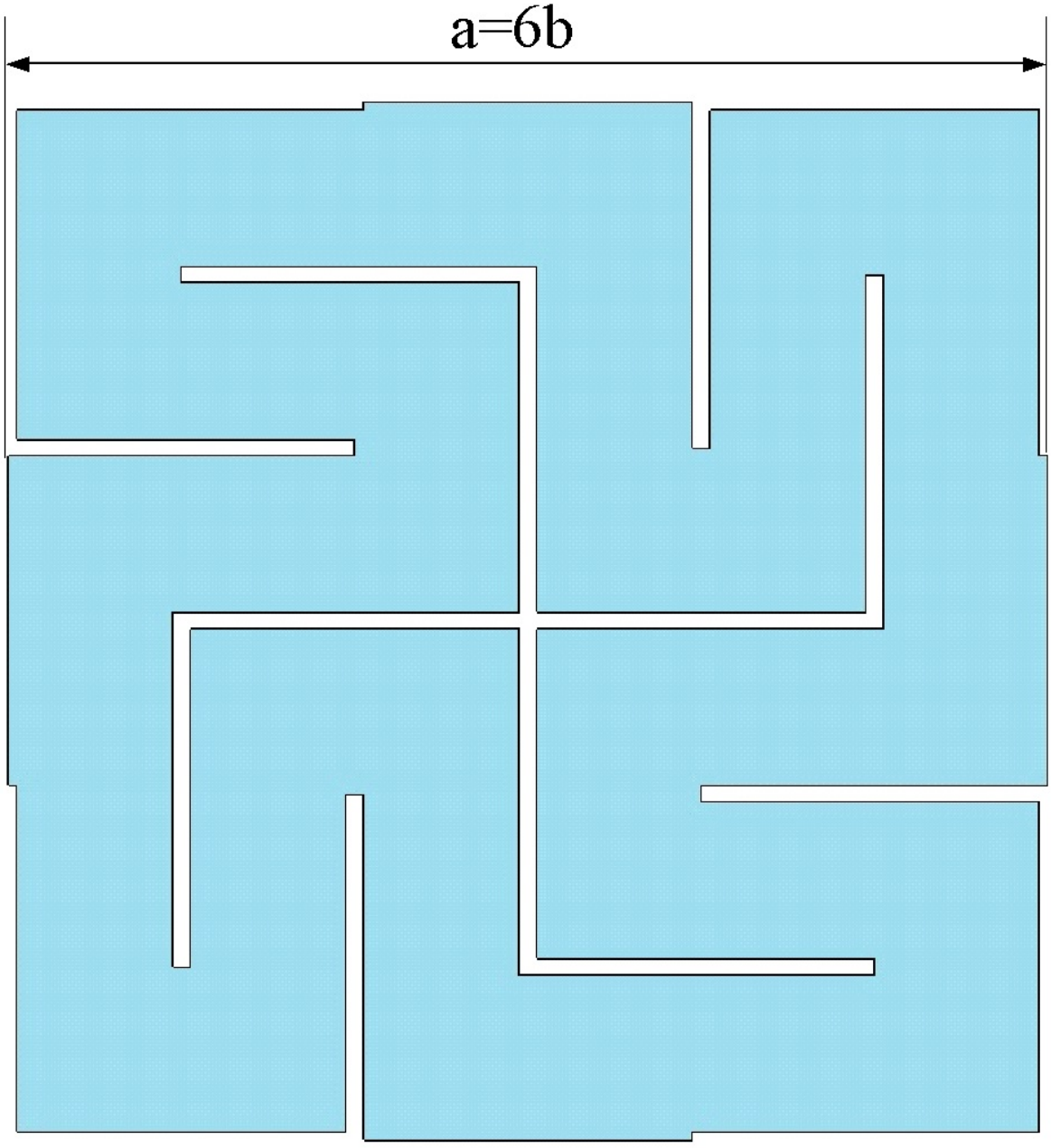

Fig. 11a

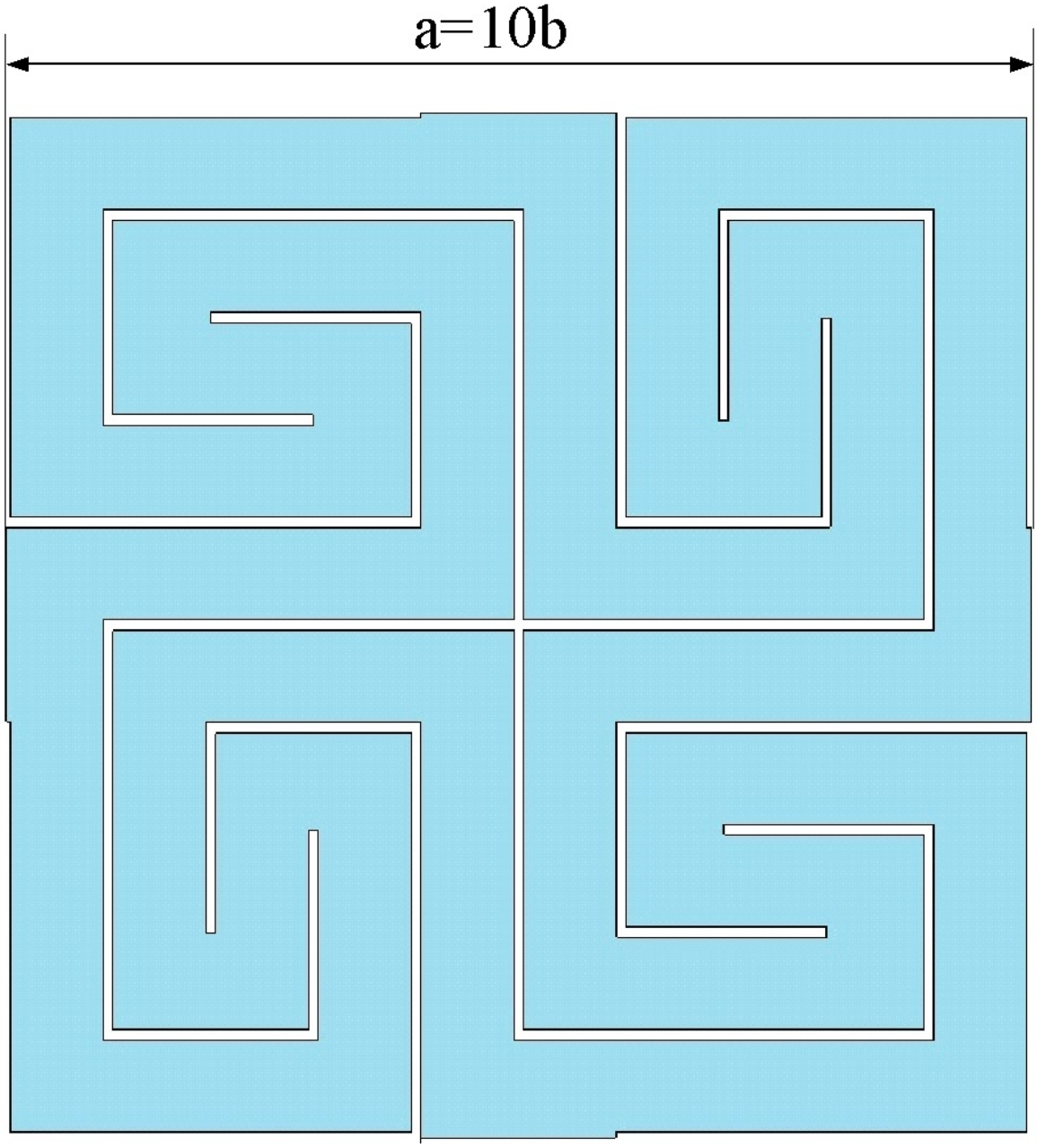

Fig. 11b

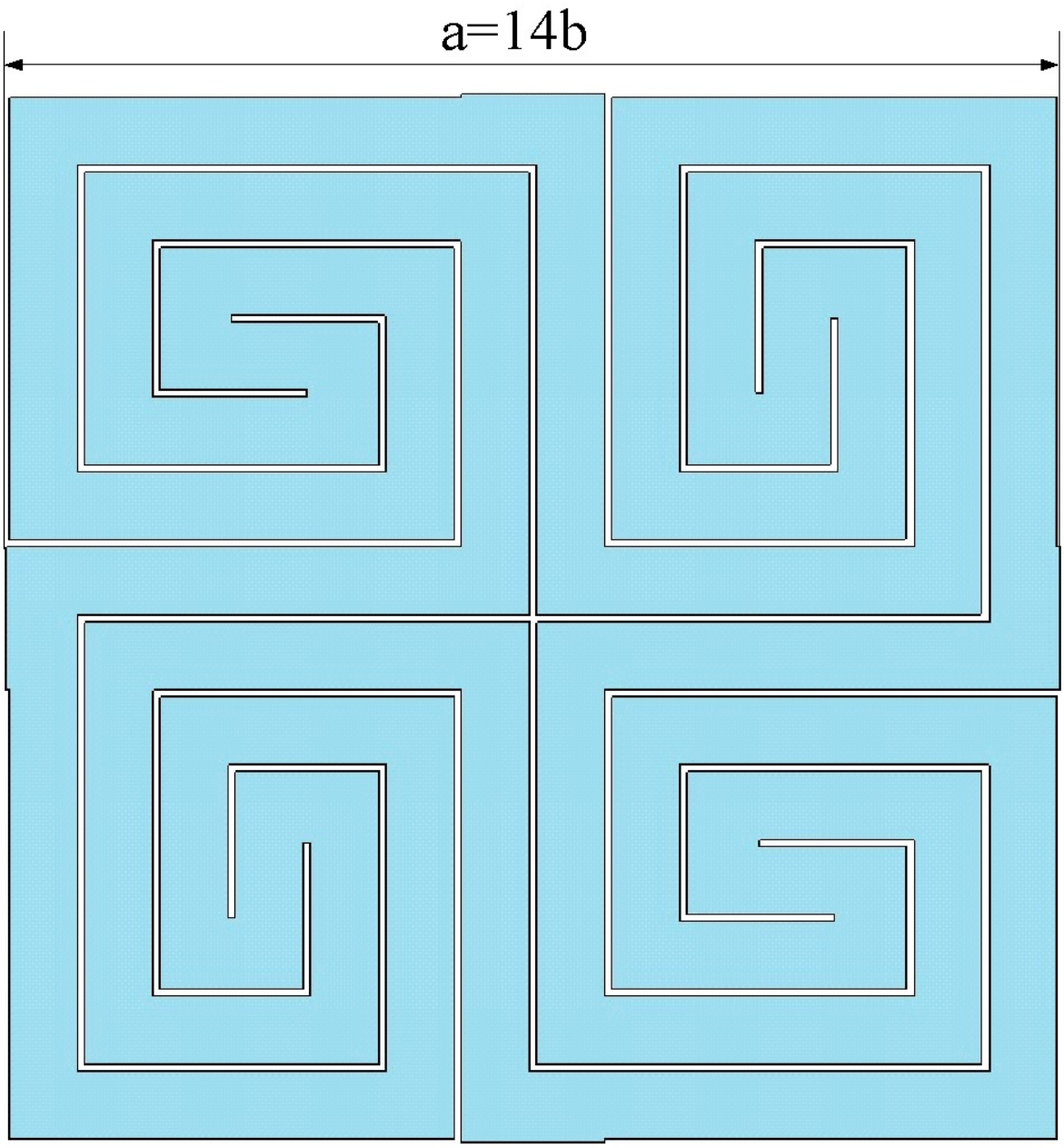

Fig. 11c

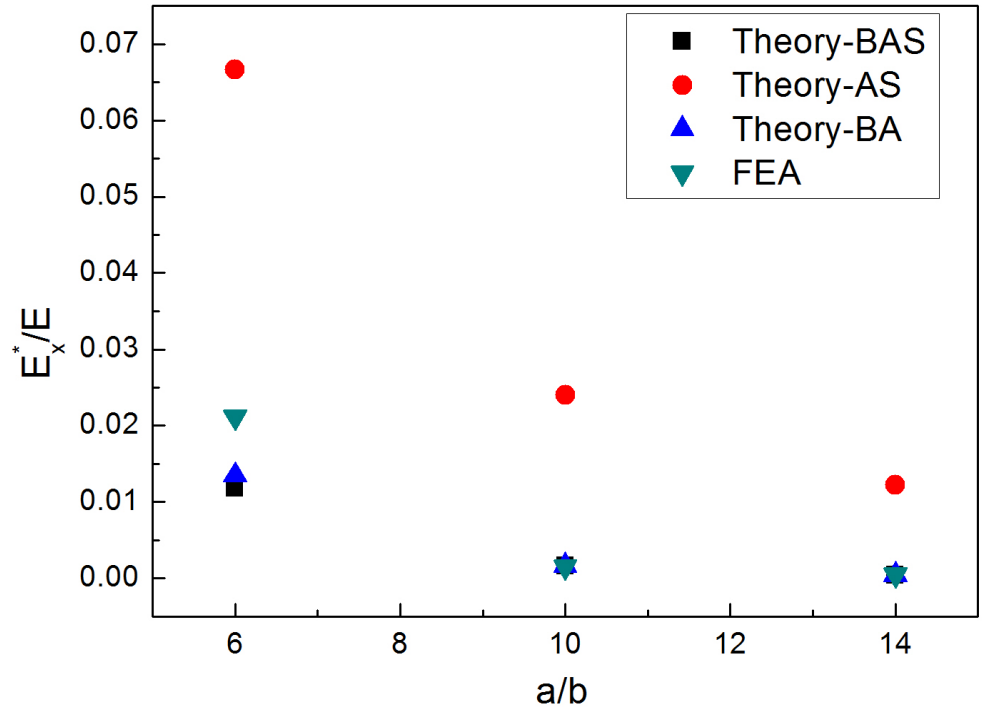

Fig. 12a

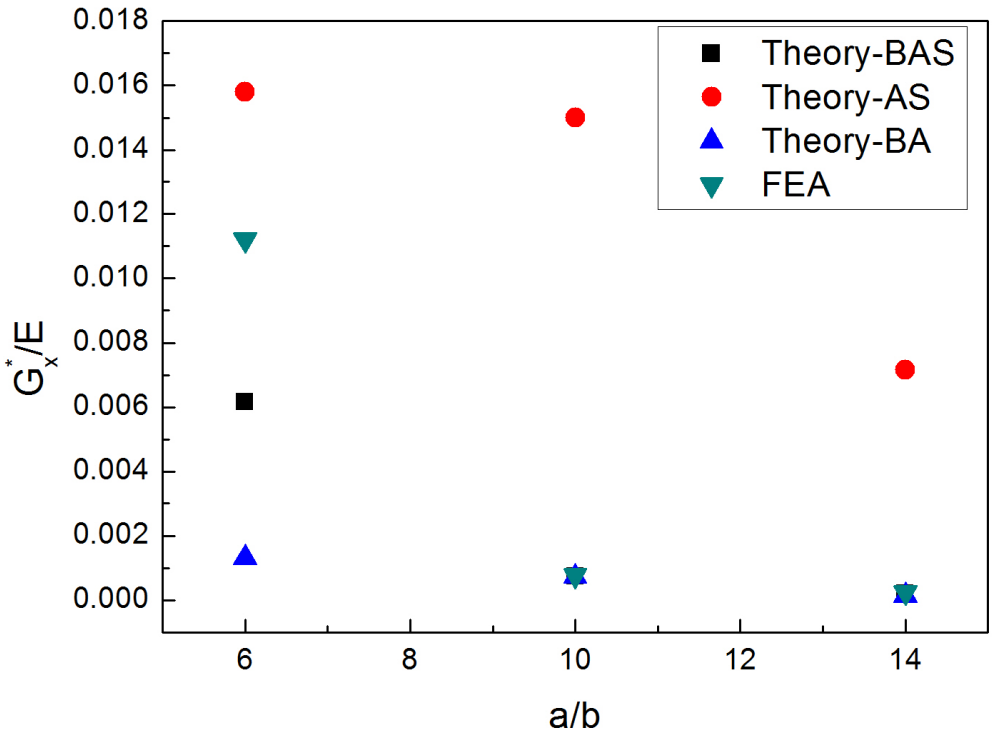

Fig. 12b

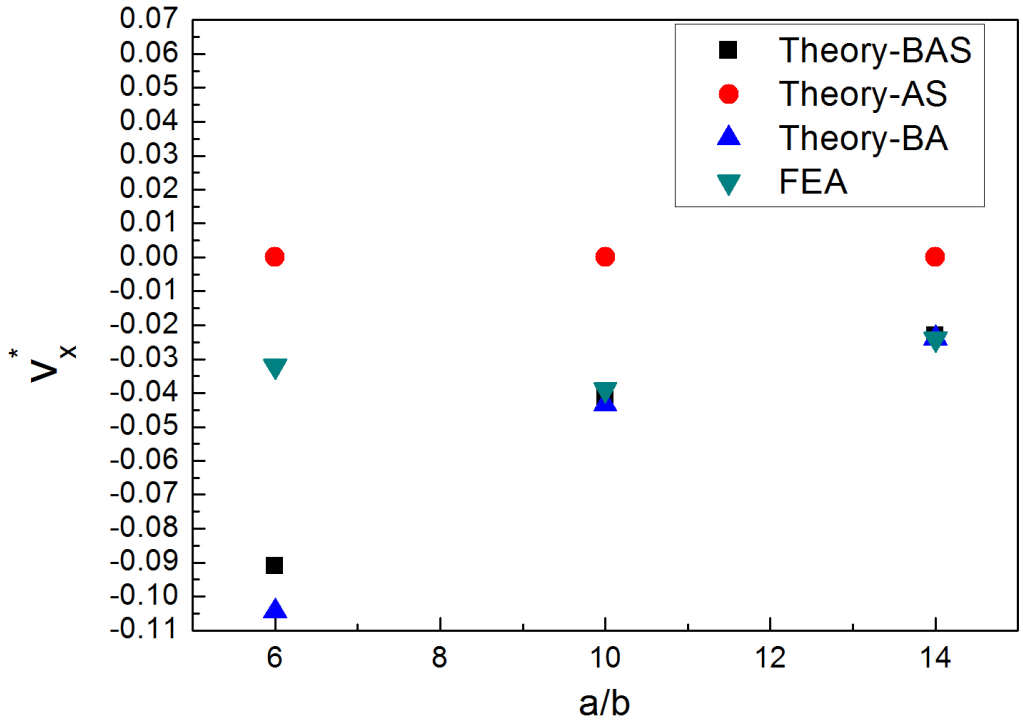
0.07
0.06
0.05
0.04
0.03
0.02
0.01
0.00
-0.01
-0.02
-0.03
-0.04
-0.05
-0.06
-0.07
-0.08
-0.09
-0.10
-0.11
V_x^*
6
8
10
12
14
a/b
Theory-BAS
Theory-AS
Theory-BA
FEA

Fig. 12c